# Evolution under dark conditions of particles from old and modern diesel vehicles, in a new environmental chamber characterized with fresh exhaust emissions

Boris Vansevenant[1,2,3]; Cédric Louis[1,2]; Corinne Ferronato[3]; Ludovic Fine[3]; Patrick Tassel[1];
Pascal Perret[1]; Evangelia Kostenidou[4]; Brice Temime-Roussel[4]; Barbara D'Anna[4]; Karine
Sartelet[5]; Véronique Cerezo[1]; Yao Liu[1]*

[1]EASE, University Gustave Eiffel, Bron, 69500, France
[2]French Agency for Ecological Transition, ADEME, 49000, Angers
[3]IRCELYON, University Claude Bernard Lyon 1, Villeurbanne, 69100, France
[4]LCE, Aix-Marseille University, UMR 7376 CNRS, Marseille, 13331, France
[5]CEREA, Joint Laboratory Ecole des Ponts ParisTech/EdF R&D, University Paris-Est, Marne-la Vallée, France

*Correspondence to*: Yao Liu (yao.liu@univ-eiffel.fr)

**Abstract.** Atmospheric particles have several impacts on health and environment, especially in urban areas. Part of those particles is not fresh, and has undergone atmospheric chemical and physical processes. Due to a lack of representativeness in experimental conditions, and experimental artifacts such as particle wall losses in chambers, there are uncertainties on the effects of physical processes (condensation, nucleation and coagulation), and their role in particle evolution from modern vehicles. This study develops a new method to correct wall losses, accounting for size-dependence and experiment-to-experiment variations. It is applied to the evolution of fresh diesel exhaust particles to characterize the physical processes which they undergo. The correction method is based on the black carbon decay and a size-dependent coefficient to correct particle distributions. Six diesel passenger cars, Euro 3 to Euro 6 were driven on a chassis dynamometer with Artemis Urban cold start and Artemis Motorway cycles. Exhaust was injected in an 8 $m^3$ chamber with Teflon walls. The physical evolution of particles was characterized during 6 to 10 hours. Condensation occurs even without photochemical reactions, due to the presence of intermediate volatility organic compounds and semi-volatile organic compounds. These compounds were quantified at emission, and induce a particle mass increase up to 17 %.$h^{-1}$, mainly for the older vehicles (Euro 3 and Euro 4). Condensation is 4 times faster when the available particle surface if multiplied by 3. If initial particle number concentration is below $[8-9] \times 10^4$ #.$cm^{-3}$, it can increase up to 25 %.$h^{-1}$ due to nucleation or condensation on particles below 14 nm. Above this threshold, particle number concentration decreases due to coagulation, up to -27 %.$h^{-1}$.

## 1. Introduction

Air pollution is a major concern due to its impacts on climate, environment and health. It has been classified as carcinogenic to humans by the International Agency for Research on Cancer (IARC, 2016). Its effects are greater in urban areas, where pollutants such as fine particles accumulate and present a serious health risk due to human exposure. Road traffic is an important source of particles in urban environments (Rivas et al., 2020). Many particle-emitting vehicles such as old diesel cars are still present on roads of several countries (EEA, 2020).

Freshly emitted particles and gases undergo physical evolutions in the atmosphere, such as nucleation, coagulation and condensation (Seinfeld and Pandis, 2016). Chemical reactions in the gas phase, enhanced by oxidative processes and photochemistry, form organic compounds with lower volatility (Seinfeld and Pandis, 2016). These compounds can undergo the physical processes of condensation and nucleation, leading to Secondary Organic Aerosols (SOA). SOA is estimated to contribute to 50-85 % of the Organic Aerosol (OA) burden (Zhu et al., 2017), and to 30-77 % of $PM_{2.5}$ during haze pollution in China (Huang et al., 2014). Numerous studies focus on particle evolution and SOA formation in the presence of added oxidants and strong UV lights (Chen et al., 2019; Chu et al., 2016; Lambe et al., 2011; Lu et al., 2019; Sbai et al., 2020; Wang et al., 2018b). They aim at characterizing the photooxidation processes of organic compounds during several hours. This might not be thoroughly representative of all atmospheric conditions (Chen et al., 2019). Several situations exist in which particles evolve with limited light (winter rush hours, nighttime, tunnels), and exposure may occur close to traffic (Harrison et al., 2018), shortly after emissions. In those situations, some physical evolutions took place, but not yet oxidation/photooxidation processes. Some studies focused on physical processes only (Giechaskiel et al., 2005; Harrison et al., 2018; Jeong et al., 2015; Kozawa et al., 2012; Morawska et al., 2008; Zhang et al., 2004; Zhang and Wexler, 2004). They are mainly based on the measurement of particles near freeways or from vehicles exhaust plume. These methods enable the study of emissions in real conditions, but are impacted by the presence of external sources and high dilution due to the wind and distant measurement. The presence of external sources (cooking, building, heater, wood burning, biogenic sources…) creates a mixture with the traffic emission. It induces difficulties to evaluate the impact of traffic on atmospheric aerosol. Moreover, few of these studies were conducted in the last decade, resulting in a lack of knowledge on modern vehicles, motorizations and aftertreatment technologies. Some studies focusing on particle physical evolution use a constant volume sampler (CVS) (Louis et al., 2017), but they are limited by the short residence time.

Moreover, the physical processes of condensation and nucleation depend in part on concentrations of gas-phase particle precursors, such as Semi-volatile and Intermediate-Volatility Organic Compounds (SVOCs and IVOCs, respectively). IVOCs can participate in physical evolutions and SOA formation (Sartelet et al., 2018; Xu et al., 2020), but their quantification is impacted by sampling methodology. The uncertainties arise from the effects that dilution and temperature have on the gas-particle partitioning. They also come from the chemical identification to quantify total IVOCs (Xu et al., 2020; Zhao et al., 2015, 2016). This results in a lack of knowledge on their emissions and on the effect of motorization and aftertreatment technologies (Drozd et al., 2019; Zhao et al., 2015). This also impacts the understanding of their role in particle evolutions and the accuracy of atmospheric models (Sartelet et al., 2018; Zhao et al., 2018). More investigations should consequently be conducted to characterize the IVOC and SVOC emissions from modern vehicles equipped with different aftertreatment technologies. The particle physical evolutions during several hours and under controlled experimental conditions should also be investigated. The studies focusing only on vehicle emissions are complementary to those performed near freeways with presence of other sources and with photochemistry. This would help better understand the actual contribution of road traffic to particle pollution.

Laboratory studies on particle evolutions are often performed in atmospheric chambers. They are a good mean of investigating the physical processes of nucleation, condensation and coagulation. The study of those processes requires information on particle concentrations, size and distributions (Leskinen et al., 2015; Nah et al., 2017; Pierce et al., 2008; Wang et al., 2018a). However, these parameters are affected by leakage and wall deposition

due to Brownian diffusion, gravitational settling, turbulence and electrostatic charge of the Teflon walls (Leskinen et al., 2015; Nah et al., 2017; Pierce et al., 2008; Seinfeld and Pandis, 2016; Wang et al., 2018a, 2014). Leakage and wall deposition of particles induce a decrease in particle mass over time. This prevents the

80   analysis of the mass evolutions from condensation or evaporation of organic material onto or from pre-existing particles. Moreover, since wall deposition depends on particle diameter, it affects the distribution evolutions and therefore the ability to quantify the role of coagulation. It also affects the observation of nucleation mode particles. Particle data in chambers therefore need to be corrected for leakage and wall losses.

Some studies (Grieshop et al., 2009; Nah et al., 2017; Pathak et al., 2007) have used size-independent wall losses

85   correction methods. It is usually done with the help of a tracer, such as black carbon, assumed to be reliable, and enabling the consideration of the experiment-to-experiment variations. However, particle wall losses are known to be size-dependent (Charan et al., 2018; La et al., 2016; Leskinen et al., 2015; Pierce et al., 2008; Wang et al., 2018a; Weitkamp et al., 2007). The use of the same correction coefficient to the whole distribution can mislead the observation of processes such as coagulation. Other studies have therefore used size-dependent correction

90   methods (Nah et al., 2017; Pierce et al., 2008; Wang et al., 2018a). They enable a more precise analysis of the processes affecting the size distribution. However, those methods are usually based on the decay of ammonium sulphate particles (Wang et al., 2018a). They assume that their loss rates are the same as those of the studied particles. Furthermore, the loss rate studies cannot be conducted simultaneously with the actual experiments. They are therefore usually carried out before and after the campaign, thus preventing the experiment-to-

95   experiment variations from being accounted for (Wang et al., 2018a).

Firstly, this study presents the characterization of a new 8 m$^3$ cubic chamber with Teflon walls, aimed at studying the physical particle evolutions from a wide range of on-road vehicles. Six diesel vehicles (2 without diesel particle filter (DPF) Euro 3 and Euro 4; 3 Euro 5 with additive DPF or catalyzed DPF; 1 Euro 6 with additive DPF and selective catalytic reducer (SCR)) were tested to develop the new leakage and size-dependent

100  wall loss correction method. Five gasoline vehicles (3 with port fuel injection Euro 3, 4 and 5; 2 Euro 5 with direct injection) were also used. The new leakage and wall loss correction method is based on the complementarity of a tracer (black carbon) and a size-dependent equation to correct wall losses. It accounts for experiment-to-experiment variations.

Secondly, this study presents the emissions and evolutions of particles from the 6 diesel vehicles, Euro 3 to

105  Euro 6, in urban and motorway conditions. Emission factors (EFs) of particle number (PN), particle mass (PM), black carbon (BC), non-methane hydrocarbons (NMHCs) and IVOCs are estimated. They are used to discuss the impact of aftertreatment technologies on emissions and particle evolutions. Moreover, the results of the diesel particle physical evolutions in the chamber under dark conditions are presented. Data are corrected for leakage and wall losses using the new correction method. The physical processes are characterized in the dark in order to

110  better understand their share in particle evolution mechanisms. This study is complementary to those focusing on photochemical processes, to better evaluate the total contribution of road traffic to atmospheric particle pollution.

Atmospheric
Measurement
Techniques
Discussions

## 2. Methods

### 2.1. Chassis dynamometer

115 The vehicles are tested on a chassis dynamometer, used to reproduce different driving conditions. The 2 non-power wheels are fixed to the floor, while the 2 power wheels are placed on a rotating 48" roller. The speed can go up to 200 km.h$^{-1}$, and is given by the driving guide in front of the vehicle. The dynamometer can apply traction or resistance to the wheels to reproduce the effects of inertia, vehicle load, slope, rolling resistance and aerodynamic resistance. A ventilation system is placed in front of the vehicle to avoid over heating of the engine. The air is blown with a flow proportional to the vehicle speed to cool the engine similarly as it would be on road.

### 120 2.2. Artemis cycles

The vehicles are tested with the Artemis Urban Cold start (UC) cycle and the Artemis Motorway (MW) cycle (André, 2004). They represent specific driving conditions, typical of urban environments and highways, and are chosen to simulate emissions found within big cities (small streets and urban highways). The speed profiles are given in Fig. A1 for the UC cycle and the MW cycle.

### 125 2.3. Vehicles

Dynamometer tests are performed with diesel and gasoline passenger cars (PCs), whose characteristics are given in Table 1. Six diesel vehicles are used in this study: 2 vehicles without DPF, Euro 3 (D1) and Euro 4 (D2); 3 Euro 5 vehicles, 2 with an additive DPFs (D3 and D4) and 1 with a catalyzed DPF (D5); and 1 Euro 6 vehicle (D6) equipped with an additive DPF and a SCR. Five gasoline vehicles are tested: 3 with port fuel injection 130 (PFI), G1 to G3 with standards Euro 3, 4 and 5; 2 Euro 5 with direct injection (DI), G4 and G5.

**Table 1: Characteristics of the diesel and gasoline vehicles used in this study for the chamber characterization and the particle evolution.**

| Diesel vehicles | | | | | | |
|---|---|---|---|---|---|---|
| **Vehicle** | **D1** | **D2** | **D3 (add DPF)** | **D4 (add DPF)** | **D5 (cat DPF)** | **D6 (add DPF and SCR)** |
| **Standard** | Euro 3 | Euro 4 | Euro 5 | Euro 5 | Euro 5 | Euro 6 |
| **Mass (kg)** | 1290 | 1085 | 1080 | 1515 | 1200 | 1090 |
| **Mileage (km)** | 191612 | 95982 | 105823 | 103000 | 85617 | 43919 |
| **Aftertreatment technologies** | DOC[1] | DOC | DOC + add DPF[2] | DOC + add DPF | DOC + cat DPF | DOC + SCR[3] + add DPF |

| Gasoline vehicles | | | | | |
|---|---|---|---|---|---|
| **Vehicle** | **G1 (PFI)** | **G2 (PFI)** | **G3 (PFI)** | **G4 (DI)** | **G5 (DI)** |
| **Injection** | PFI[4] | PFI | PFI | DI[5] | DI |
| **Standard** | Euro 3 | Euro 4 | Euro 5 | Euro 5 | Euro 5 |
| **Mass (kg)** | 1185 | 1170 | 1030 | 1100 | 1285 |
| **Mileage (km)** | 195305 | 95096 | 27712 | 97089 | 92550 |
| **Aftertreatment technologies** | TWC[6] | TWC | TWC | TWC | TWC |

[1] DOC = Diesel Oxidation Catalyst
[2] DPF = Diesel Particle Filter
[3] SCR = Selective Catalyst Reducer
[4] PFI = Port Fuel Injection
[5] DI = Direct Injection
[6] TWC = Three-Way Catalyst

Atmospheric
Measurement
Techniques
Discussions

Open Access

EGU

### 2.4.  Exhaust gas sampling and injection into the chamber

135   Exhaust gas is sampled from the tailpipe by an ejector dilutor (Dekati L7, Sapelem 50 NL.min$^{-1}$, Sapelem 1 NL.min$^{-1}$). The dilutor works with air which is dehumidified, filtered using HEPA particle filters and activated carbon, and heated at 120 ° using a Fine Particle Sampler (FPS Dekati, 4000). Exhaust gas is diluted between 3 and 20 times, depending on air pressure and ejector dilutor type. The air and exhaust gas are injected into the chamber at the height of 90 cm, through a 2 to 4 m long stainless-steel line. The line is heated at 120 °C to avoid

140   condensation and deposition on its inner surface. The heated line is cleaned after each injection with hot dry clean air, during a couple of hours.

### 2.5.  Environmental chamber

The study of the exhaust particle evolution is performed inside the University Gustave Eiffel UGE 8 m$^3$ cubic chamber. The structure of the chamber is made of aluminum, and the walls are made with a 70 µm thin Teflon

145   film, used because chemically inert. However, it can be electrostatically charged and influence the wall deposition of gas and particles inside the chamber. The theoretical total volume is 8000 L, but it can vary (± 300 L) due to deformation of the walls, depending on inner pressure. To avoid contamination from the outside, the chamber is always kept at a slight overpressure (~ 5 Pa) by injection of clean air. This also compensates the losses by leakage and instrument sampling. This injection induces dilution inside the chamber.

150   The temperature, humidity and relative pressure are continuously monitored. Instruments sample the air of the chamber at the center, at 5 different heights: 20 cm, 60 cm, 100 cm, 140 and 180 cm.

### 2.6.  Cleaning

Before the first experiment, the inner walls of the chamber were cleaned by hand with microfiber cloth. While this removes most particles and gaseous species on the walls, it also induces high electrostatic charge due to

155   friction of the cloth on Teflon. Manual cleaning was therefore only done once. At the end of each experiment, cleaning is performed with injection of dry clean air, with flowrates varying between 150 and 300 L.min$^{-1}$. Cleaning lasts a minimum of 12 hours, thus renewing the air inside the chamber at least 13 times. Since dilution induces an exponential decrease of the pollutant concentrations, this gives a minimum theoretical percentage of clean air inside the chamber of 99 %.

160  ### 2.7.  Instruments

#### 2.7.1.  Gas-phase analysis

Non-Methane Hydrocarbons (NMHCs) are measured either directly from the tailpipe with a Horiba Portable Emissions Measurement System (PEMS) or after a CVS by flame ionization detection with a Horiba analysis system.

165   IVOCs are collected from the heated line (prior injection into the chamber) by sampling diluted exhaust through stainless steel tubes filled with Tenax TA at a flow rate of 45 mL.min$^{-1}$. The samples are collected during the entire driving cycle. Collected samples are further analyzed by Automatic Thermal Desorption coupled with Gas Chromatography-Mass Spectrometry detector (ATD-GC-MS). The Markes Unity thermodesorber and a GC6890 gas chromatograph from Agilent fitted with the MS5973 mass spectrometer from Agilent are used. The thermal

170   desorption system consists in a 2-stage desorption. During the first desorption step, the compounds are desorbed

by heating the Tenax TA under a stream of helium and are condensed on a trap filled with adsorbent and maintained at -5 °C. During the second desorption, the second trap is flash-heated to 300 °C for a rapid introduction of the compounds into the chromatographic column. The chromatographic column used is an Agilent HP1MS 30 m × 0.25 mm, 0.25 µm. The mass spectrometer operates in scanning mode at an electron

175 ionization of 70 eV. Mass spectral data are acquired over a mass range of 33-450 amu. Qualitative identification of compounds is based on the match of the retention time and confirmed by matching their mass spectra with those of standards and from the NIST mass spectral library. Quantification is conducted by the external standard method. Known amount (1 µL) of standard solutions of volatile organic compounds (VOCs) and IVOCs are introduced into cleaned Tenax TA tubes, using an automatic heated GC injector. The calibration tubes are

180 analyzed in the same conditions as mentioned before. The chromatogram shows an unresolved complex mixture, mainly composed of co-eluted hydrocarbons which cannot be further separated by a single-dimensional GC. The alkanes (linear and branched) are quantified by SIR-based response factor of these compounds using the fragment of $m/z=57$. The response factor used for quantification of branched alkanes is the one of the compound with the same number of carbon as its parent chain. The fragment $m/z=83$ is used for the quantification of

185 cyclohexane and of the other cyclic compounds. The fragment $m/z=78$ is used for the quantification of benzene, and $m/z=91$ for other aromatics. The fragment $m/z=128$ is used for the quantification of naphthalene. The compounds from the standard solutions taken for quantification of each identified compound are listed in Table 2. The use of response factors from different compounds than the identified ones can induce some error in their quantification. Over the whole range of IVOCs, this error is estimated to be below 8 % (7.8 % and 0.4 %

190 respectively for 2 urban cycles). For single SVOCs, the errors range from 90 to 98 %. Since all compounds above C22 are quantified using compounds with different carbon numbers (C20 for vehicles D1, D5, and C16 for vehicles D2, D3, D6), the impact on their quantification is important. They are however of the same order for all vehicles, and allow comparison between vehicles and driving conditions.

195 **Table 2: List of the compounds from the standard solutions whose response factors were chosen for quantification of the identified compounds, for vehicles D1, D4 and D5 as well as vehicles D2, D3 and D6. The identified alkanes are sorted by number of carbon atoms in their parent chain: C12 to C16, C17 to C20 and C>20.**

| Identified compounds | Compounds from standard solutions whose response factor were taken for quantification | |
| --- | --- | --- |
| | Vehicles D1 and D5 | Vehicles D2, D3 and D6 |
| n-alkanes C12 to C16<br>b-alkanes with parent chain C12 to C16 | dodecane<br>tridecane<br>tetradecane<br>pentadecane<br>hexadecane | dodecane<br>tridecane<br>tetradecane<br>pentadecane<br>hexadecane |
| n-alkanes C17 to C20<br>b-alkanes with parent chain C17 to C20 | heptadecane<br>octadecane<br>nonadecane<br>eicosane | hexadecane |
| n-alkanes C>20<br>b-alkanes with parent chain C>20 | eicosane | hexadecane |
| naphthalene | naphthalene | toluene |
| cycloalkanes in the IVOC retention time range | cyclohexane | R-cyclohexane |
| aromatics in the IVOC retention time range with C≤9 | branched benzene (C9) | branched benzene (C9) |
| aromatics in the IVOC retention time range with C≥10 | branched benzene (C10) | branched benzene (C10) |

Atmospheric
Measurement
Techniques
Discussions

Linear (n-) and branched (b-) alkanes are classified according to their number of carbon C as an indicator of their effective saturation concentration, according to Zhao et al. (2015). Alkanes with C<12 are considered as VOCs, alkanes from C12 to C22 are considered as IVOCs, and alkanes with C>22 are considered as SVOCs. Also

200  according to Zhao et al. (2015), IVOCs are considered to be the sum of n- and b- alkanes (from C12 to C22), naphthalene, as well as aromatics and cycloalkanes in the same retention time bin as C12-C22 alkanes.

The $CO_2$ concentration is measured from the chamber using a MIR2M (Environment SA), which samples air at 1.5 L.min$^{-1}$. The temporal resolution is 1 second, and the analytical uncertainty is 0.001 %.

### 2.7.2.    Particle-phase analysis

205  Particle concentrations and size distributions are measured with a Scanning Mobility Particle Sizer (SMPS, TSI), composed of an advanced aerosol neutralizer (3087), a Differential Mobility Analyzer (DMA, 3081) column, and a Condensation Particle Counter (CPC, 3775). The sampling flow is 0.3 L.min$^{-1}$. Classification is based on the particle electrical mobility, and the measurement range goes from 14 to 615 nm. The particle mass is computed, with the assumption that particles are spherical, with an arbitrary density of 1.2 (Barone et al., 2011;

210  Totton et al., 2010). Data are given with a 5 minute time scale, with a 5 % analytic uncertainty.

The black carbon concentration is measured using an AE33-7 aethalometer from Magee Scientific. Air is sampled at 2 L.min$^{-1}$ on filter tape. The black carbon concentration is given by absorption measurements at 880 nm (Andreae and Gelencser, 2006). Data are given with a time-scale of 1 minute.

### 2.8.    Ammonium sulphate experiments

215  In order to test the wall losses correction method with non-volatile inert seeds, experiments are performed with ammonium sulphate particles. Particles are generated from diluted solutions using an atomizer aerosol generator (TSI, 3079A) at a flow rate of 5 L.min$^{-1}$ during 20 min to 2.5 hours. After injections, particles reached concentrations ranging from 5500 to 50600 #.cm$^{-3}$. Characteristics of these experiments are given in Table 3.

**Table 3: Characteristics of the ammonium sulphate experiments.**

| Concentration of solution (mg.L$^{-1}$) | Injection duration (min) | Initial [PN][1] (#.cm$^{-3}$) | Initial [PM][2] (#.cm$^{-3}$) | Initial mode (nm) |
|---|---|---|---|---|
| 25.0 | 33 | 5589 | 0.5 | 40.0 |
| 50.0 | 60 | 8100 | 0.9 | 40.0 |
| 10.0 | 24 | 19197 | 2.3 | 41.4 |
| 50.0 | 120 | 37931 | 7.2 | 59.4 |
| 10.0 | 167 | 50622 | 17.2 | 68.5 |

220  [1] [PN] = Particle Number concentration       [2] [PM] = Particle Mass concentration

### 2.9.    Sum up of the experiments

Table 4 summarizes the experimental conditions for the 6 diesel and the 5 gasoline vehicles. Most experiments are performed under similar conditions and are repeated at least twice. For the D4 and the G3 vehicles, different conditions are tested. The line was heated once at 80 °C instead of 120 °C, showing no specific influence on

225  particle concentration in the chamber. Also, different ejector dilutions are tested, and show a great impact on the initial particle concentrations in the chamber. An ideal dilution of 8.4 is found, leading to total dilution in the

chamber between 65 and 130. It is considered ideal for the sake of this study since it enables to have diluted exhaust giving particles concentrations covering a wide range, depending on emissions. This variety in initial particle concentration is important to study the influence of initial concentration on particle evolution.

230  **Table 4: Sum up of the conditions for the diesel and gasoline experiments.**

| Vehicle | Standard | Line temp (°C) | Ejector dilution | Artemis Urban Cold Start | | Artemis Motorway | |
|---|---|---|---|---|---|---|---|
| | | | | Number of cycles | Total dilution | Number of cycles | Total dilution |
| Diesel vehicles | | | | | | | |
| D1 | Euro 3 | 120 | 8.4 | 2 | 97 | 3 | 65 |
| D2 | Euro 4 | 120 | 8.4 | 2 | 97 | 3 | 130 |
| D3 (add DPF) | Euro 5 | 120 | 8.4 | 2 | 97 | 2 | 65-130 |
| D4 (add DPF) | Euro 5 | 80-120 | 2.3-15.0 | 2 | 19-387 | 1 | 26 |
| D5 (cat DPF) | Euro 5 | 120 | 8.4 | 2 | 97 | 2 | 65 |
| D6 (add DPF and SCR) | Euro 6 | 120 | 8.4 | 1 | 97 | 1 | 65 |
| Gasoline vehicles | | | | | | | |
| G1 (PFI) | Euro 3 | 120 | 8.4 | 1 | 97 | 3 | 65 |
| G2 (PFI) | Euro 4 | 120 | 8.4 | | | 1 | 130 |
| G3 (PFI) | Euro 5 | 120 | 2.3-8.4 | 3 | 19 | 4 | 13-130 |
| G4 (DI) | Euro 5 | 120 | 8.4 | 2 | 97 | 2 | 130 |
| G5 (DI) | Euro 5 | 120 | 8.4 | 2 | 97 | 1 | 130 |

### 2.10.  Chamber characterization

#### 2.10.1.  Mixing time

During injection inside the chamber, turbulence is induced due to the flow of exhaust gas, and the mixture is not homogeneous right after the end of injection. Moreover, to avoid the increase of particle deposition surface and

235  turbulence (Crump et al., 1982; Nomura et al., 1997), there is no fan system to make the mixture homogeneous. To determine the necessary time to have a homogeneous mixture inside the chamber, $CO_2$ is injected, and the concentration is measured at 3 of the 5 sampling heights of the chamber: the bottom one (20 cm), the middle one (100 cm) and the top one (180 cm). The average concentration over the 5 sampling heights is also monitored during injection of $CO_2$.

240  #### 2.10.2.  Leakage

Leakage describes the loss of pollutants and air due to overpressure, through the corners and door of the chamber. The leak rate is quantified experimentally using 2 complementary methods. The first method, called "pressure method", uses injection of air inside the chamber. A constant flow of air is injected at a precise value. Simultaneously, pressure is monitored, and when it gets stable, it means that the flow or air exiting the chamber

245  (e.g. leak flow) is the same as the one injected. This experiment is realized with different flow rates from 0.1 L.min$^{-1}$ up to 6.0 L.min$^{-1}$.

The second method uses measurement of the $CO_2$ concentration, and is referred to as the "$CO_2$ method". High concentrations of $CO_2$ are injected inside the chamber, and the concentration decay is observed at constant

Atmospheric
Measurement
Techniques
Discussions

Open Access

EGU

pressure. This method was used by Papapostolou et al. (2011) with the CO decay. The $CO_2$ concentration
decreases exponentially due to dilution by compensation of air injected into the chamber, and to leakage at a
given relative pressure varying between 0.17 Pa and 18.42 Pa. The decay coefficient is converted into a leak
flow, expressed in L.min$^{-1}$, thus allowing comparison with the "pressure-method" results. The leak flow ($F_{leak}$)
can also be expressed as a leak rate ($Rate_{leak}$), given as the percentage of the total volume exiting the chamber in
1 hour, according to Eq. (1).

$$Rate_{leak}(\%vol.h^{-1}) = \frac{100 \times 60 \times F_{leak}}{8000} \tag{1}$$

### 2.10.3. Wall losses

The leakage and size-dependent wall loss correction method presented in this study is based on 4 consecutive
steps. Step 1 consists in correcting total [PM] using the decay of the black carbon concentration [BC]. During
step 2, the particle distribution is corrected using a size-dependent wall loss coefficient. This coefficient is based
on the theory of Crump and Seinfeld (1981), with an arbitrary estimation of the turbulence. Step 3 consists in
optimizing the turbulence parameter $k_e$ to fit corrected data with results of step 1. Finally, step 4 is the
computation of the total particle number and mass corrected concentrations.

- **Step 1: [PM] correction using [BC]**

The first step consists in correcting the total particle mass, using BC as a tracer for primary particle emissions, as
done by Grieshop et al. (2009). As BC is an inert compound (Platt et al., 2013; Wang et al., 2018a), the decay of
its concentration is due to leakage and wall deposition, with a loss rate $k_{BC}$. By assuming that particles are
internally mixed, total particle mass has the same loss rate as BC (Grieshop et al., 2009; Hennigan et al., 2011;
Platt et al., 2013). A corrected PM concentration can thus be obtained at all times of each experiment (Grieshop
et al., 2009; Hennigan et al., 2011; Platt et al., 2013) with Eq. (2).

$$[PM]_{corrected}^{step1}(t) = [PM]_{measured}(t) \times \exp(k_{BC} \times t) \tag{2}$$

For some experiments, the decay of [BC] cannot accurately be fitted by a 1$^{st}$ order exponential decay. In those
cases, the term $\exp(k_{BC}t)$ is replaced by $[BC]_{t0}/[BC]_t$.

This corrected concentration $[PM]_{corrected}^{step1}(t)$ represents the evolution of particle mass due to nucleation or
condensation/evaporation of organic material. Particles lost to the walls are assumed to be at equilibrium with
suspended ones (Grieshop et al., 2009).

- **Step 2: Particle-size-dependent correction**

The second step consists in correcting particle mass and number concentration, accounting for the size-
dependence of wall deposition (Charan et al., 2018; Leskinen et al., 2015; Pierce et al., 2008; Wang et al., 2018b,
2018a). The aerosol wall deposition rate due to turbulent diffusion, Brownian diffusion and gravitational
sedimentation is given in Eq. (3) (Corner and Pendlebury, 1951; Crump and Seinfeld, 1981). It is given for a
cubic chamber of side length L, as a function of particle diameter $D_p$.

$$\beta_i(D_p) = \frac{1}{L} \times \left[ \frac{8\sqrt{\frac{k_e D(D_p)}{\pi}}}{\pi} + v(D_p) \times \coth\left( \frac{\pi v(D_p)}{4\sqrt{k_e D(D_p)}} \right) \right] \tag{3}$$

280    With:

- i the SMPS particle size channel of geometric midpoint diameter $D_p$

- $k_e$ the eddy diffusivity coefficient (sec$^{-1}$)

- $D(D_p) = \frac{k_{boltz} T C_c}{3\pi\mu D_p}$ the Brownian diffusivity (m$^2$.sec$^{-1}$)

- $v(D_p) = \frac{D_p^2 \rho_p g C_c}{18\mu}$ the terminal particle velocity (m.sec$^{-1}$)

285    - $C_c$ the Cunningham slip-correction factor $C_c = 1 + \frac{2\lambda}{D_p} \times \left[ 1.257 + 0.4 \times \exp\left( -\frac{1.1 \times D_p}{2\lambda} \right) \right]$

All terms of this equation, except for $k_e$, can be found using literature (Crump and Seinfeld, 1981; Seinfeld and Pandis, 2016) and experimental data. They are listed in Appendix B. The $k_e$ coefficient represents the turbulence inside the chamber, induced by the exhaust gas injection, the air flow to compensate leakage and sampling, and electrostatic forces near the walls (Charan et al., 2018; Crump and Seinfeld, 1981; Pierce et al., 2008; Seinfeld

290    and Pandis, 2016; Wang et al., 2018a). As it cannot be measured (Charan et al., 2018), $k_e$ will in a first instance be given an arbitrary value in order to compute $\beta_i$ ($D_p$). The rate of leakage is taken as defined by Schnell et al. (2006) as the ratio of the flows entering (or exiting) the chamber $\dot{V}$ by the volume of the chamber V: $\alpha = \dot{V}/V$. It follows similar basis to the "pressure method" defined above. It assumes that at constant pressure, the flow of air injected into the chamber is equal to the sum of leakage and of what is sampled by the instruments. It is

295    determined for each experiment, using the flow of air injected into the chamber $\dot{V}$ (L.sec$^{-1}$) and the total volume of the chamber V. The loss of particles due to leakage and wall deposition in each size bin can then be estimated for the arbitrary value of $k_e$. Assuming that the coefficients α and $\beta_i$ ($D_p$) are constant over the course of each experiment, the loss process is a first-order exponential decay (Leskinen et al., 2015; Nah et al., 2017; Pierce et al., 2008; Verheggen and Mozurkewich, 2006; Wang et al., 2018a, 2018b, 2014) given by Eq. (4).

$$[PM_i]_{lost}^{step2}(t)\big|_{arbitrary\ k_e} = [PM_i]_{measured}(t_0) \times \left(1 - e^{-(\alpha+\beta_i)\times t}\right) \tag{4}$$

300    By adding this to the measured distribution at time t ($[PM_i]_{measured}(t)$), a distribution corrected for leakage and wall deposition can be obtained. It represents the particle mass distribution evolution, solely due to photochemical and physical processes (Eq. (5)).

$$[PM_i]_{corrected}^{step2}(t)\big|_{arbitrary\ k_e} = [PM_i]_{measured}(t) + [PM_i]_{lost}^{step2}(t) \tag{5}$$

The corresponding total mass concentration can be computed with Eq. (6). The factor 64 comes from the fact that multiple charge corrections are based on a 64-channel resolution (TSI, 2010).

$$[PM]_{corrected}^{step2}(t)\big|_{arbitrary\ k_e} = \frac{\sum [PM_i]_{corrected}^{step2}(t)\big|_{arbitrary\ k_e}}{64} \tag{6}$$

305    • **Step 3: Optimization using least square error algorithm**

Atmospheric
Measurement
Techniques
Discussions

So far, the evolution of the total particle mass corrected for leakage and wall deposition has 2 different expressions. They both represent the evolution of total particle mass in the chamber solely due to photochemical and physical processes of nucleation and condensation (coagulation can also occur, but has no effect on particle mass). However, the expression obtained during step 2 ($[PM]_{corrected}^{step2}(t)|_{arbitrary\ k_e}$) is attached to high

310    uncertainties as it is found for an arbitrary value of $k_e$. Charan et al. (2018) realized an optimal fitting of experimental data to determine the parameter $k_e$. Following the same idea, an optimization of $k_e$ is performed to minimize the difference between the corrected PM concentrations obtained during step 1 (considered as the reference) and during step 2 (Eq. (7)).

$$\sum_{t=t_0}^{t=t_{final}} \left\{ [PM]_{corrected}^{step1}(t) - [PM]_{corrected}^{step2}(t)|_{optimized\ k_e} \right\}^2 \xrightarrow{k_e} minimum \qquad (7)$$

This operation results in an optimized expression of $\beta_i\ (D_p)$, for each chamber experiment. It is used in the

315    equations of step 2 (Eq. (3), Eq. (4), Eq. (5), Eq. (6)), to obtain corrected distributions and total concentrations. The values of $\beta_i\ (D_p)$ are used to compute a mean wall loss coefficient $\beta_{ke}^{mean}$, depending on the $k_e$ value found after optimization. To account for the SMPS bins, each $\beta_i\ (D_p)$ is weighted with the relative size of the channel i ($D_p$), according to Eq. (8).

$$\beta_{k_e}^{mean} = \sum_{D_{p,min}}^{D_{p,max}} \left[ \beta_i(D_p) \times \frac{D_{p,i+1} - D_{p,i}}{D_{p,max+1} - D_{p,min}} \right] \qquad (8)$$

With:

320    -    $D_{p,i}$ the diameter associated with the bin i, with $D_p$ ranging from 14.1 nm to 615.3 nm
       -    $D_{p,i+1}$-$D_{p,i}$ the size of the bin i, where $D_{p,max+1}$=637.8 nm
       -    $\sum(D_{p,i+1} - D_{p,i}) = 623.7\ nm$ the total measurement range considered in this study

The optimized coefficient $\alpha+\beta_{ke}^{mean}$ represents the rate of particle losses due to leakage and size-dependent wall deposition.

325    • **Step 4: Corrected number distribution and number concentration**

The size-dependent optimized loss coefficient $\alpha+\beta_i\ (D_p)$ can be applied to the number distribution to determine what is lost due to leakage and wall deposition (Eq. (9)).

$$[PN_i]_{lost}(t) = [PN_i]_{measured}(t_0) \times \left(1 - e^{-(\alpha+\beta_i)\times t}\right) \qquad (9)$$

This lost distribution can be added to the measured one, to obtain a corrected number distribution (Eq. (10)). The corresponding corrected total number concentration can be computed (TSI, 2010) with Eq. (11).

$$[PN_i]_{corrected}(t) = [PN_i]_{measured}(t) + [PN_i]_{lost}(t) \qquad (10)$$

$$[PN]_{corrected}(t) = \frac{\sum [PN_i]_{corrected}(t)}{64} \qquad (11)$$

330 This method can also be used to determine the size-dependent loss rate $\beta_i$ ($D_p$) for seed only experiments, with ammonium sulphate particles. The evolution of those particles is not impacted by effects of condensation or evaporation. This means that the corrected total mass of ammonium sulphate particles should be a constant, equal to the concentration at time $t_0$, as expressed in Eq. (12). This corrected mass in used as the reference in Eq. (7) of step 3. The mass concentration decay is associated to a rate $k_{PM}^{amm\ sul}$, which represents the losses due

335 to leakage and wall deposition only. It can therefore be compared to the rate $k_{BC}$ found for exhaust particle experiments.

$$[PM]_{corrected}^{step1}(t) = [PM]_{measured}^{seed\ only}(t_0) \tag{12}$$

## 3.     Results

### 3.1.     Chamber characterization

#### 3.1.1.     Mixing time

340 Mixing time is investigated using $CO_2$ measurements at 3 sampling heights as presented in Figure 1a. They show that just 1 min after the end of the $CO_2$ injection, the vertical gradient of $CO_2$ is important. The mean $CO_2$ concentration is $0.977 \pm 0.013$ %, but this value reaches 0.964 % at the top of the chamber and 0.990 % at the bottom. After 20 minutes, the mean concentration is $0.972 \pm 0.003$ %, with a minimum value of 0.969 % at the top and 0.975 % at the bottom. From that time, the concentration variability is less than 1 % between the

345 minimum and maximum values, and the mixture can be considered homogeneous. After 1 hour, the mixture is homogeneous if the instrument uncertainties are accounted for.



**Figure 1: Determination of the mixing time in the chamber, using injection of $CO_2$, with measurements of the concentration at 3 different heights 1 min, 20 min and 60 min after injection (a), and with evolution of the average**
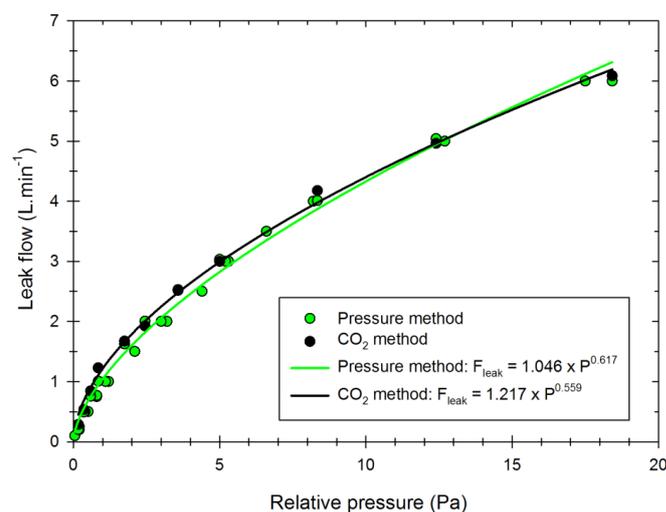350 **concentration during 60 min after injection (b).**

The $CO_2$ concentration averaged over the 5 sampling heights is shown in Figure 1b. Results show that the mean concentration increases rapidly during the first 20 minutes following injection. Then it reaches its maximum and remains stable. At this stage, the mixture can be considered as homogeneous.

Atmospheric
Measurement
Techniques
Discussions
Open Access
EGU

The results of the $CO_2$ tests indicate that the mixture inside the chamber can be considered as homogeneous 20
355    minutes after the end of injection. Therefore, in this study, all the chamber analysis will start 20 minutes after the
end of the exhaust gas injection.

### 3.1.2. Leakage

The leak flows obtained with the "pressure method" and the "$CO_2$ method" are presented in Figure 2 with the
green and black curves respectively.



360

**Figure 2 : Values of the leak flow as a function of relative pressure, obtained with the "pressure method" (green) of
the "$CO_2$ method" (black). The dots represent the experimental results, and the curves represent the mathematical
simulation for both methods.**

Both methods give similar results. A numerical fit of the curves gives a mathematical expression (Eq. (13)) for
365    the leak flow $F_{leak}$ (L.min$^{-1}$) as a function of the relative pressure $\Delta P$ (Pa) between the chamber and outside.

$$F_{leak}(L.min^{-1}) = (1.13 \pm 0.12) \times \Delta P^{0.59 \pm 0.04} \tag{13}$$

For values of relative pressure between 0.2 and 5 Pa, the leak flow is between 0.4 and 2.9 L.min$^{-1}$, corresponding
to a leak rate between 0.3 and 2.2 %vol.h$^{-1}$. Platt et al. (2013) reported for the PSI chamber an average leak rate
of 0.08 %vol.h$^{-1}$. This is lower than the one found in this study, probably due to fact that the chamber is operated
under overpressure conditions. This leak rate can be used to estimate gas and particle phase leakage from the
370    measured relative pressure. For this study, a leak rate is estimated for each experiment, without the dependency
on the relative pressure. Indeed, it can change between the end of injection and the remaining of the chamber
experiment (the leakage due to high overpressure measured right after injection is not accounted for, but
decreases rapidly). Another leak definition is given in the wall losses section, with similar basis as the "pressure
method", and taking into account the instruments sampling flows.

### 375    **3.1.3.    Wall losses**

The 4-step correction method is applied to more than 50 experiments using particles from passenger car exhausts (diesel or gasoline) and ammonium sulphate particles. The associated experimental protocols are described in the part Methods. The optimization processes give $k_e$ values between 0.001 and 27.32 sec$^{-1}$, with an average of 2.41 sec$^{-1}$. The corresponding wall loss coefficients are respectively $1.05 \times 10^{-4}$, $1.58 \times 10^{-2}$ and $4.69 \times 10^{-3}$ min$^{-1}$ for

380    a particle of diameter 100 nm. These values are similar to those reported by Leskinen et al. (2015) and Babar et al. (2017), of $7.50 \times 10^{-4}$ and $3.96 \times 10^{-3}$ min$^{-1}$, respectively. Figure 3 shows the size distribution of the wall loss coefficient $\beta_i (D_p)$ as well as the corresponding mean wall loss coefficient $\beta_{ke}^{mean}$ for 3 values of $k_e$ in this range: $k_e = 0.36$ sec$^{-1}$; $k_e = 2.57$ sec$^{-1}$; $k_e = 16.70$ sec$^{-1}$. These values are chosen to represent the lower part of the range, the average, and the upper part of the range, respectively. The mean wall loss coefficients are respectively

385    $1.31 \times 10^{-3}$ min$^{-1}$; $8.44 \times 10^{-3}$ min$^{-1}$; and $2.13 \times 10^{-2}$ min$^{-1}$.
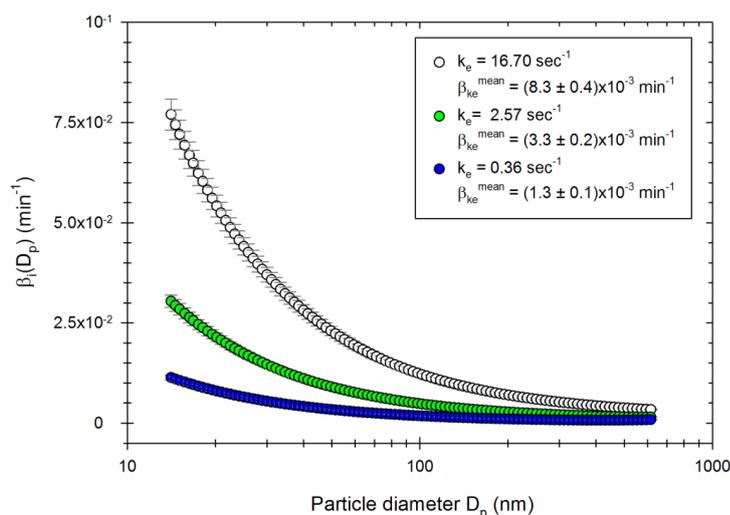


**Figure 3: Distribution of the wall loss coefficient $\beta_i (D_p)$ for 3 values of $k_e$ obtained experimentally: 16.70 sec$^{-1}$ (white); 2.57 sec$^{-1}$ (green) and 0.36 sec$^{-1}$ (blue).**

Figure 3 shows that for a given $k_e$, wall losses vary greatly as a function of the particle diameter in the range

390    15-600 nm. They are higher for smaller particles, due to higher Brownian diffusion. These results also show that the wall loss coefficients are very sensitive to the parameter $k_e$. Differences increase as the particle diameters decrease. The value of the eddy diffusivity $k_e$ depends on the turbulence induced by the injection into the chamber and the electrostaticity of the Teflon walls, which can change between 2 experiments. Since experimental conditions greatly influence the turbulence and the wall deposition (Nah et al., 2017; Wang et al.,

395    2018a), it is important to account for experiment-to-experiment variations when correcting particle losses.

In about a third of the chamber experiments, total particle losses cannot be approximated by a simple exponential decay of [BC]. These experiments usually took place shortly after the chamber walls were manually cleaned. These actions resulted in an important electrostatic charge induced to the walls, thus increasing particle losses. For these "charged walls" experiments, the optimized values of $k_e$ range from 0.62 to 27.32 sec$^{-1}$, with an

400    average of 7.98 sec$^{-1}$. These values are high but still lower than some values (36 and 269.4 sec$^{-1}$) found in literature (Crump and Seinfeld, 1981; Okuyama et al., 1986). The associated values of the total loss coefficient
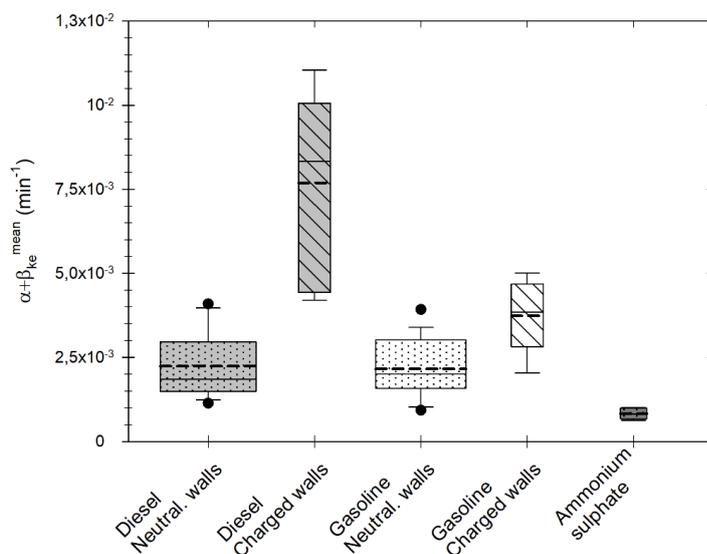
$\alpha+\beta_{ke}^{mean}$ are shown in Figure 4 with the hatched boxes, for diesel (light grey) and gasoline (white). They are in the range $[4.19\text{-}11.05]\times10^{-3}$ min$^{-1}$ for diesel and $[2.04\text{-}5.01]\times10^{-3}$ min$^{-1}$ for gasoline. Respective mean values are $7.69\times10^{-3}$ min$^{-1}$ and $3.73\times10^{-3}$ min$^{-1}$.

405 For the remaining experiments (69 %), total particle losses are well approximated by a simple exponential decay of [BC]. Values of $k_{BC}$ range from $1.11\times10^{-3}$ to $3.15\times10^{-3}$ min$^{-1}$ for vehicle exhaust experiments. Values of $k_{PM}^{amm\ sul}$ range from $5.27\times10^{-4}$ to $1.17\times10^{-3}$ min$^{-1}$ for ammonium sulphate experiments. The losses found for these experiments are lower than for the "charged walls" experiments. This is because the wall electrostatic charges have been neutralized with deposition of particles during previous experiments. The associated values of

410 $k_e$ for those "neutralized walls" experiments range from 0.04 to 3.23 sec$^{-1}$ (vehicle exhaust) and from 0.001 to 0.06 sec$^{-1}$ (ammonium sulphate). These values are in the range of what has been found in previous studies. Charan et al. (2018) found values of $k_e$ between 0.015 and 8.06 sec$^{-1}$ in simulations of wall losses in Teflon environmental chambers. The values of the total loss coefficient $\alpha+\beta_{ke}^{mean}$ associated to those "neutralized walls" experiments are shown in Figure 4 (dotted boxes), for diesel (light grey), gasoline (white) and ammonium

415 sulphate (dark grey). They are in the range $[1.25\text{-}4.09]\times10^{-3}$ min$^{-1}$ for diesel, $[0.93\text{-}3.93]\times10^{-3}$ min$^{-1}$ for gasoline and $[0.63\text{-}1.01]\times10^{-3}$ min$^{-1}$ for ammonium sulphate. Respective mean values are $2.24\times10^{-3}$ min$^{-1}$, $2.16\times10^{-3}$ min$^{-1}$ and $0.83\times10^{-3}$ min$^{-1}$. The mean $\alpha+\beta_{ke}^{mean}$ values for the "neutralized walls" experiments are 3.4 (diesel) and 1.7 (gasoline) times lower than for the "charged walls" experiments. This is close to what was found by Wang et al. (2018a), with particle loss rates 3-4 times higher between "undisturbed" and "disturbed" experiments.



420

**Figure 4: Mean loss coefficient $\alpha+\beta_{ke}^{mean}$ (accounting for channel size) for the chamber experiments performed with particles from diesel (light grey) and gasoline (white) engines, as well as ammonium sulphate particles (dark grey). Coefficients for the diesel and gasoline experiments are sorted in 2 categories: "neutralized walls" experiments for which [BC] evolution follows a simple exponential decay (dotted boxplots) or "charged walls" experiments for which**
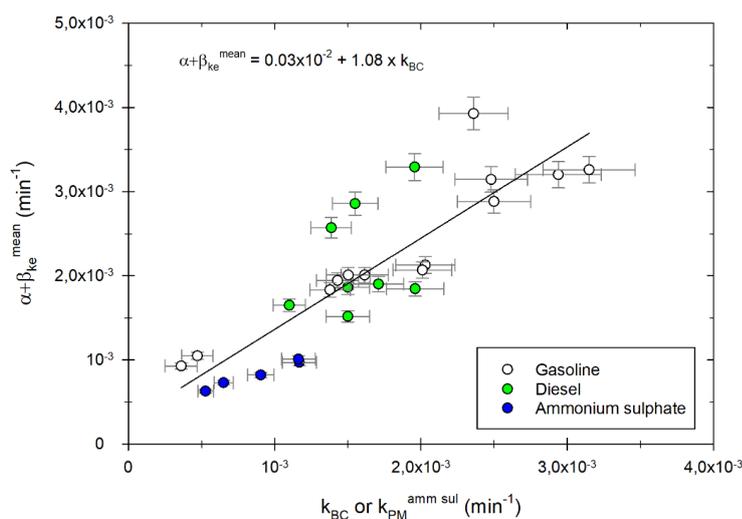425 **[BC] evolutions follows a double exponential decay (hatched boxplots). The boxes represent the 25th and 75th percentile. The solid line in the center represents the median; the dashed line represents the mean. The whiskers are the 10th and 90th percentiles. The width of the boxes is proportional to the box's data set.**

Figure 4 shows that particles from diesel and gasoline engines cover a wide range of $\alpha+\beta_{ke}^{mean}$ coefficients, especially for some diesel experiments. This is mostly due to the fact that some of those experiments took place

430    when the walls were electrostatically charged. The first experiments performed with charged walls (e.g. with the highest electrostatic charge) were with diesel engine particles.  This explains the very high values reached by the diesel "charged walls" coefficients. Ammonium sulphate particles have lower loss coefficients than engine particles, and remain in a narrow range. This could be explained by their nature and chemical composition. Also, the flow at which they are introduced in the chamber (5.6 L.m$^{-1}$) is much lower than for vehicle exhaust

435    experiments (20-60 L.min$^{-1}$). The turbulence and Brownian diffusion are therefore lower, and wall deposition decrease. For the ammonium sulphate experiments, the loss coefficient (leak + wall losses) found with the 4-step correction method range from $8\times10^{-6}$ sec$^{-1}$ to $2\times10^{-5}$ sec$^{-1}$, for particles of diameter 100 nm. Nah et al. (2017) studied the wall loss coefficient ammonium sulphate of particles in a 12 m$^3$ chamber. They found values of β at 100 nm around $1$-$5\times10^{-5}$ sec$^{-1}$. The values found in this study are in pretty good agreement with what was found

440    by Nah et al. (2017). This indicates that the correction method developed in this study gives good results, consistent with what is found for other chambers of comparable size. Figure 4 shows that the nature of the particles is likely to impact the loss coefficients. This shows the advantage of the 4-step correction method, which isn't based on the assumption that the particles of the study have the same losses as ammonium sulphate particles. Figure 4 also shows that the electrostatic state of the walls appears to be the most important factor

445    determining particle losses to the walls.

The coefficients $\alpha+\beta_{ke}^{mean}$ and $k_{BC}$ both represent the rate at which particles are lost due to leakage and wall deposition, and should in theory be correlated. To investigate this, $\alpha+\beta_{ke}^{mean}$ coefficients of "neutralized walls" experiments (e.g. for which [BC] follows a simple exponential decay giving a $k_{BC}$ coefficient) are plotted in Figure 5 as a function of $k_{BC}$ or $k_{PM}^{amm\,sul}$.



450

**Figure 5 : Mean loss coefficient $\alpha+\beta_{ke}^{mean}$ as a function of the decay coefficient $k_{BC}$ or $k_{PM}^{amm\,sul}$ obtained for the "neutralized walls" chamber experiments performed with particles from diesel (green) and gasoline (white) engines or ammonium sulphate particles (blue). A linear fit of the data is shown (black line).**

Figure 5 shows that there is a good correlation between both loss rates $\alpha+\beta_{ke}^{mean}$ and $k_{BC}$. A linear regression is

455    performed and gives a slope of $1.08 \pm 0.15$. This shows that the optimized value $\alpha+\beta_{ke}^{mean}$ gives a good representation of total losses due to leakage and wall deposition. This result indicates that the complementarity

Atmospheric
Measurement
Techniques
Discussions

Open Access
EGU

of the [PM] correction using [BC], and the size-dependent correction, is relevant. Results of Figure 5 also show that loss rates of ammonium sulphate particles are generally lower than those from diesel or gasoline experiments, as found previously (Figure 4). Even though wall charge appears as the dominant factor for particle

460    wall losses, the nature of the particles also seems to have an impact. This shows the interest of using the 4-step correction method described above.

### 3.2.    Emission factors of particles, BC and IVOCs from diesel vehicles

Vehicle emissions are quantified in order to discuss the impact of each vehicle type and driving condition on initial chamber concentration and associated physical evolutions. Emission factors of PN, PM and BC are

465    estimated from initial concentrations in the chamber by applying the dilution ratio. Moreover, since condensation and nucleation partly depend on the concentration of organic material, emissions of IVOCs and certain SVOCs are quantified. They are measured directly from exhaust to estimate the quantity of available organic material in the chamber. Finally, NMHC emissions are measured from the CVS, to discuss the share of IVOCs which is identified. Six diesel vehicles (Euro 3 to Euro 6) are tested in both UC and MW conditions. Results are shown in

470    Figure 6: EFs of PN (a), PM (b), BC (c), IVOCs (d), NMHCs (e), and the ratio (%) of the IVOC EFs over the NMHC EFs.
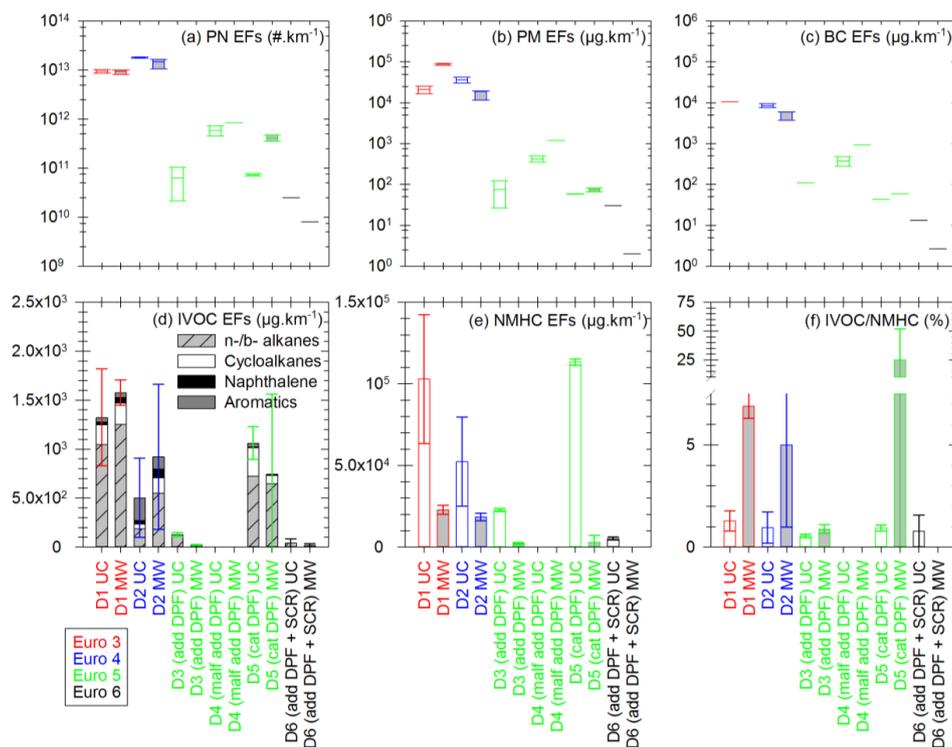


Figure 6: Emission factors of PN (a), PM (b), BC (c), IVOCs (d) and NMHCs (e), and IVOC/NMHC ratio (f) for the 6 tested Euro 3-6 diesel vehicles UC (white) and MW (light grey) conditions. IVOC EFs (d) are the sum of EFs of linear
475    and branched (n- and b- respectively) alkanes (hatched grey), cycloalkanes (white), naphthalene (black) and aromatics (dark grey), with retention times in the range corresponding to C12-C22 alkanes. EFs are given in µg.km$^{-1}$, and the IVOC/NMHC ratio in %. Vehicles are sorted by Euro norm: Euro 3 in red; Euro 4 in blue; Euro 5 with add or cat DPF in green and Euro 6 in black. The Euro 5 vehicle showing signs of malfunctioning DPF is referred to as

Atmospheric
Measurement
Techniques
Discussions

480 **"D4 (malf add DPF)". The boxes represent the 25th and 75th percentile. The solid line in the center represents the median. The whiskers are the 10th and 90th percentiles. Error bars represent 1 standard variation on figures (d) to (f). Figure (f) has a broken axis to better show the smaller values.**

Figure 6 shows that PM and BC EFs have a good correlation for all vehicles and driving conditions, with slightly higher emissions for PM than BC. BC accounts on average for $(62 \pm 34)$ % of PM, which is consistent with particle composition. The Euro 3 (D1) and Euro 4 (D2) vehicles emit more PN, PM and BC than the Euro 5 (D3,

485 D4, D5) and Euro 6 (D6) ones, with factors 10–70000 (PN), 10–50000 (PM) and 4–4000 (BC). In urban conditions the Euro 5 (D3 to D5) vehicles EFs of BC, PN and PM cover a large range of values. This can be explained by the diversity and proper functioning of aftertreatment technologies for this category of vehicles (cat and add DPFs). DPFs are more effective at a certain exhaust temperature, usually not reached during a cold start urban cycle. This can lead to variations in the particle emissions. The Euro 5 vehicle with cat DPF (D5) shows

490 PN emissions much higher in MW than in UC conditions (factor 5.7). For those cycles, the PN mode is below 19 nm, which could indicate a DPF regeneration.

IVOC and NMHC EFs are the highest for the Euro 3 (D1), Euro 4 (D2), and Euro 5 with cat DPF (D5) vehicles. They are in the range 501–1576 µg.km$^{-1}$ and $(3–113)\times10^3$ µg.km$^{-1}$ for IVOCs and NMHCs respectively. IVOC emissions from the Euro 5 vehicle with cat DPF (D5) are 5.3 times and 26.8 times higher than those from the

495 vehicles with add DPFs (the Euro 5 D3 and the Euro 6 D6, respectively). The additive and catalyzed DPFs seem to have different impacts on IVOC and NMHC emissions. In UC conditions, the Euro 3 vehicle (D1) emits more IVOCs than the add DPF Euro 5 vehicle (D3) and the cat DPF vehicle (D5), with respective factors 10.7 and 1.2. This is close to what was reported by Zhao et al. (2015), with a ratio 7 in creep conditions between cat DPF-equipped and nonaftertreatment vehicles. Moreover, the driving conditions also impact IVOC emissions. For the

500 DPF-equipped vehicles, IVOC EFs are 1.4 to 6.2 times higher in UC conditions than in MW conditions. This is due to more complete combustion at high temperature operations. This follows the same trend as what was reported by Zhao et al. (2015) for diesel vehicles, with ratios from 6 to 23 between creep/idle and high speed conditions. For the Euro 3 (D1) and the Euro 4 (D2) vehicles, IVOC emissions are respectively 1.2 and 1.8 times higher in UC conditions. This could be due to the cold start.

505 Moreover, for non-DPF vehicles (D1 and D2), IVOC emissions are dominated by n- and b- alkanes, which account for 64 %. Naphthalene accounts for 6 % of IVOC emissions. Cycloalkanes and aromatics account respectively for 14 and 16 % of IVOC emissions. These results are consistent with those obtained by Lu et al. (2018) and Zhao et al. (2015). They found IVOC emissions of non-DPF diesel vehicles to be dominated by cyclic compounds and alkanes (mainly unspeciated), with also a fraction of aromatics. For the cat DPF vehicle

510 (D5), alkanes represent 78 % of IVOCs, followed by cycloalkanes (19 %) and then aromatics and naphthalene (2 and 1 % respectively). For the vehicles with add DPFs (D3 and D6), only alkanes are identified in the IVOC retention time range.
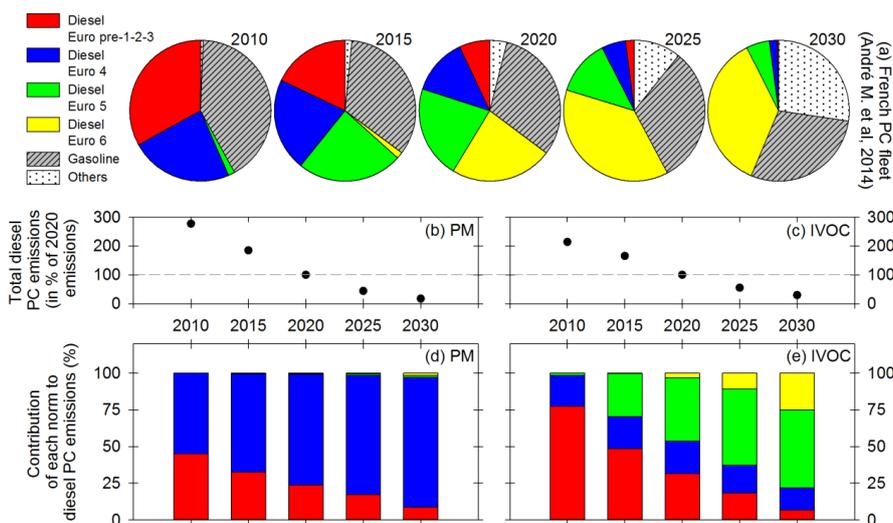
The IVOC/NMHC ratios range from $(0.5 \pm 0.1)$ % to $(6.9 \pm 0.6)$ % for all vehicles, except for the cat DPF Euro 5 (D5) one in MW conditions, with a ratio of $(24.7 \pm 27.1)$ %. The possible regeneration observed from PN

515 emissions for this vehicle in MW conditions could explain high IVOC emissions, and therefore a high IVOC/NMHC ratio. The average IVOC/NMHC ratio is $(3.5 \pm 2.9)$ % for the vehicles without DPF (D1 and D2), and $(0.8 \pm 0.2)$ % for the DPF-equipped vehicles (D3, D5, D6), without the possible regeneration value. This is substantially lower than the values of $(60 \pm 10)$ % and $(150 \pm 80)$ % found by Zhao et al. (2015), respectively for nonaftertreatment and DPF-equipped diesel vehicles. However, respectively only about $(8.1 \pm 2.3)$ % and

520    $(5.6 \pm 3.1)$ % of the total IVOC mass given by Zhao et al. (2015) was identified. This brings the IVOC/NMHC ratios to $(4.9 \pm 2.2)$ % (nonaftertreatment) and $(8.4 \pm 9.1)$ % (DPF-equipped), if considering only the identified portion of IVOCs. This is higher than what is found in this study, but remains in the same range if uncertainties are accounted for.

Certain n- and b- alkanes corresponding to SVOCs are also sampled on the sorbent tubes. Their emissions are

525    higher for the Euro 3 (D1), Euro 4 (D2) and cat DPF Euro 5 (D5) vehicles, with average EFs of 1093 and 1520 µg.km$^{-1}$ in UC and MW conditions respectively. For the Euro 5 (D3) and Euro 6 (D6) vehicles, both equipped with add DPFs, the average SVOC EFs are 263 and 247 µg.km$^{-1}$ in UC and MW conditions respectively. However, their quantification is performed with response factors from compounds with different carbon numbers (C20 for vehicles D1, D5 and C16 for vehicles D2, D3, D6). This can induce important

530    uncertainties in their EFs.

Considering the French fleet (André M. et al., 2014) and EFs of Figure 6, the contribution of each Euro norm to particle and IVOC emissions from diesel passenger cars is estimated. Since no vehicle of norms pre-Euro, Euro 1 and Euro 2 was tested, their emissions are assumed to be in the same range as those from Euro 3 vehicles. They are grouped in a category named Euro pre-1-2-3. Figure 7a gives the French passenger car fleets from 2015 to

535    2030 (André M. et al., 2014). Figure 7b and Figure 7c give the evolution of total PM and IVOC emissions, computed as the product of emission factors and fleet composition (assuming a constant number of vehicles). Figure 7d and Figure 7e show the contribution of each Euro norm to total diesel passenger car emissions of PM and IVOCs.



540    **Figure 7. Evolution of the French passenger car fleet (a) given by André M. et al. (2014), for diesel vehicles of norm Euro pre-1-2-3 (red), Euro 4 (blue), Euro 5 (green) and Euro 6 (yellow), as well as gasoline vehicles (hatched grey) and vehicles with other motorization like hybrid or electrical (dotted white). Total emissions of PM (b) and IVOCs (c) by diesel PCs, given as % of the 2020 emissions. Contribution of each Euro norm to diesel PC emissions of PM (d) and IVOCs (e). Results are given for the years 2010, 2015, 2020, 2025 and 2030.**

545    Results show that total diesel PC emissions decrease by a factor 15.8 for PM and 7.2 for IVOCs between 2010 and 2030, assuming the total number of vehicles remains constant. This is due to evolution in the PC fleet composition, with diesel vehicles representing 58 % of the PC fleet in 2010, 65 % in 2020 and 44 % in 2030.

Atmospheric
Measurement
Techniques
Discussions

Moreover, the share of more polluting diesel PCs (Euro pre-1-2-3 and Euro 4) evolves, representing 56 % of the
fleet in 2010, 20 % in 2020 and 2 % in 2030. However, due to their much higher PM emissions (compared to
550   Euro 5 and Euro 6 diesel vehicles), their share in total PM emissions remains dominant: almost 100 % in 2010,
99 % in 2020 and still 97 % in 2030.

For IVOCs, emissions are also due to DPF-equipped vehicles (Euro 5 and Euro 6). The share of those vehicles in
IVOC emissions by diesel PCs is less than 1 % in 2010, 46 % in 2020 and 78 % in 2030. More modern vehicles
will be the main contributor to IVOC emissions in 2030, with effects on particle physical and photochemical
555   evolutions. More investigations should therefore be conducted to estimate their emissions and evolutions.

### 3.3.    Evolution of particles from diesel exhaust

In this part, the physical processes having effects on particle number, mass and size are investigated, for the 6
diesel vehicles (Euro 3 to Euro 6) in both UC and MW conditions. Data are corrected for leakage and wall
losses, using the new 4-step correction method. Figure 8a gives the hourly increase of [PM], for the vehicles
560   classified by Euro norm. It shows that the Euro 3 and Euro 4 vehicles have the higher [PM] hourly increases.
Increases are at least of 5 %.h$^{-1}$ during more than 500 min, and up to 17 %.h$^{-1}$ during 100 minutes for the Euro 3.
The Euro 4 vehicle has hourly [PM] increases in the same range, and undergoes an increase during an average of
400 minutes. This increase in [PM] can be explained by condensation of organic material onto preexisting
particles. The emissions of IVOCs observed in Figure 6 for the Euro 3 and Euro 4 vehicles seem to confirm this
565   explanation. The IVOC emissions from the Euro 5 vehicles could explain the slight increase in particle mass
during evolution, presented in Figure 8a. This increase for the Euro 5 vehicles can go up to 5 %.h$^{-1}$ during almost
5 hours. The Euro 6 vehicle however, does not undergo any [PM] increase, which is consistent with the very low
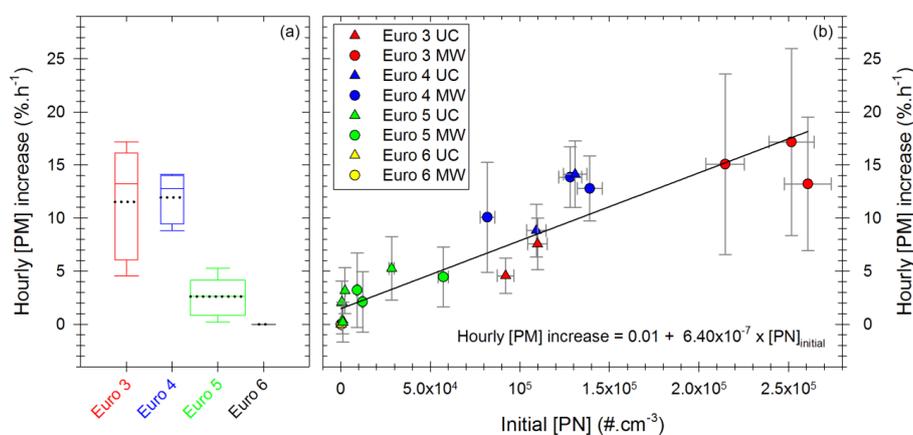emissions of precursors.



570   **Figure 8: Particle mass hourly increase in % of initial [PM] per hour. Results in (a) are given for all the diesel vehicles
sorted by Euro norm. The boxes represent the 25th and 75th percentile. The solid line in the center represents the
median; the dashed line represents the mean. The whiskers are the 10th and 90th percentiles. The width of the boxes is
proportional to the data set of the box. Results in (b) are given as a function of initial [PN] for all Euro norms (Euro 3
in red; Euro 4 in blue; Euro 5 in green; Euro 6 in yellow or black) and in both UC (triangles) and MW (circles)
575   conditions. A linear fit of the data is performed (black line) with equation written in figure (b). Error bars on figure
(b) represent 1 standard variation.**

Figure 8b shows the [PM] hourly increase as a function of initial [PN]. A linear correlation appears, indicating that conditions with large amounts of particles initially are more likely to lead to an increase in [PM]. The high hourly [PM] increases (5-17 %.h$^{-1}$) are mainly due to Euro 3 and Euro 4 vehicles, whereas Euro 5 and Euro 6

580   vehicle experiments results in lower [PM] increases (0-5 %.h$^{-1}$). This trend is consistent with the PN EFs observed in Figure 6a, since [PM] increases and initial [PN] seem to be correlated. The correlation could be explained by the fact that high initial [PN] usually result in high probability for organic material to find available surface for condensation. The presence of organic material is a limiting factor, which could also explain (Figure 6) why the Euro 6 (D6) and the add DPF Euro 5 (D3) vehicles have [PM] increases around 0.

585   In addition to the hourly [PM] increase, the time during which condensation occurs is an important piece of information. Results giving the time needed to reach the maximum of PM concentration are displayed in Figure 9a. It is plotted as a function of the initial particle surface, and the labels give the hourly [PM] increase.
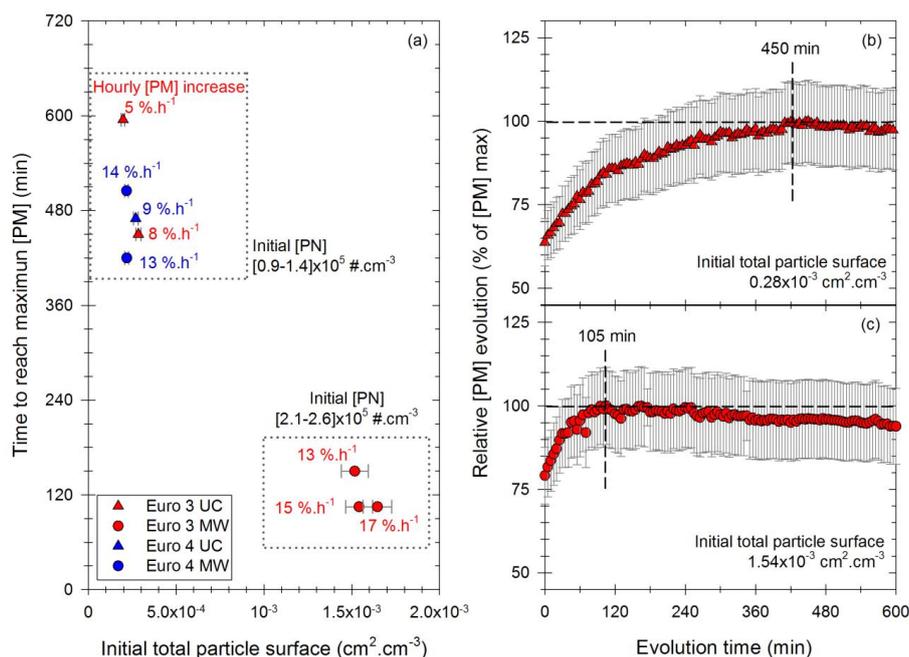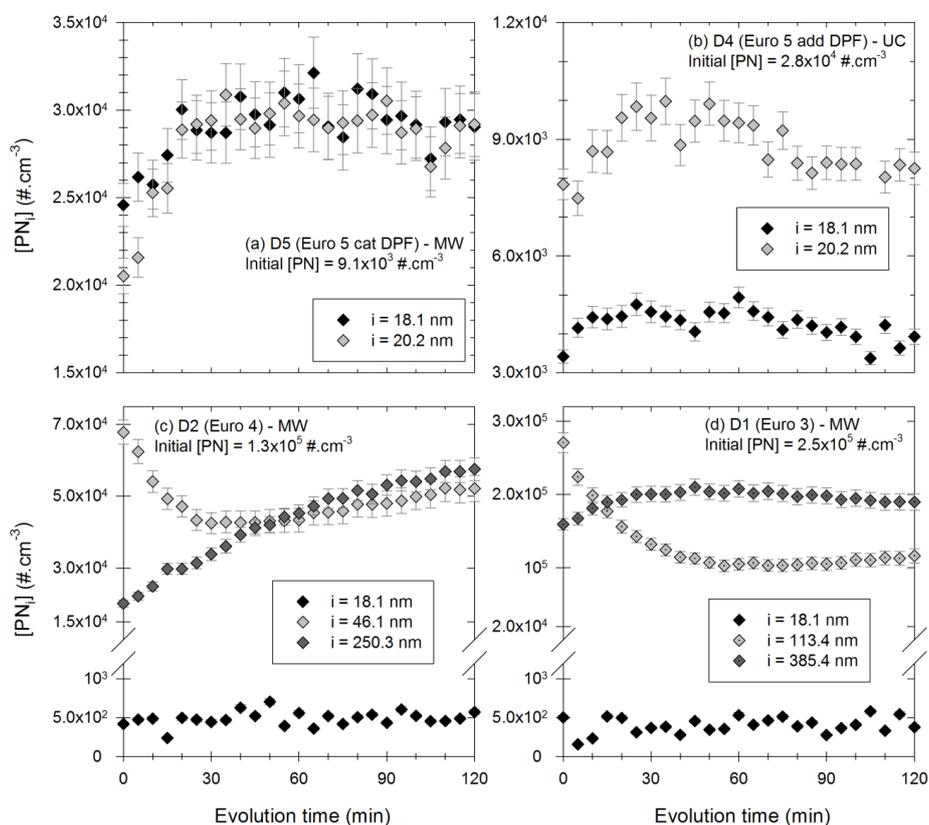


**Figure 9: Results of the study of the [PM] evolution in the chamber for experiments showing a significant increase**
590   **with the Euro 3 (red) and the Euro 4 (blue) vehicles, in UC (triangles) or MW (circles) conditions. Figure (a) gives the time to reach the maximum of [PM] as a function of initial total particle surface. Each point has a label giving the hourly [PM] increase in % of initial [PM] per hour. Two groups are found: the first one (top) for initial [PN] between 0.9 and 1.4×10$^5$ #.cm$^{-3}$; the second one (bottom) for initial [PN] between 2.1 and 2.6×10$^5$ #.cm$^{-3}$. Figures (b) and (c) give 2 examples of those [PM] evolutions with time, plotted as relative evolution of the maximum [PM]. Examples are**
595   **taken: (b) from the first group of figure (a) with initial surface of 0.28×10$^{-3}$ cm$^2$.cm$^{-3}$ and a maximum [PM] reached in 450 min; and (b) from the second group of figure (a) with initial surface of 1.54×10$^{-3}$ cm$^2$.cm$^{-3}$ and a maximum [PM] reached in 105 min.**

Figure 9 clearly shows that when the available particle surface is high (> 10$^{-3}$ cm$^2$.cm$^{-3}$), the time to reach the maximum [PM] is quite short, and doesn't exceed 2.5 hours. However, for initial surfaces below

600   4×10$^{-4}$ cm$^2$.cm$^{-3}$, condensation seems to be a very slow process. Even though uncertainties become large after 6 hours of evolution, it seems that condensation can occur slowly during 7 to 10 hours. This difference between fast and slow [PM] increases is shown in Figure 9b and Figure 9c, for 2 examples of [PM] evolution with time.

Atmospheric
Measurement
Techniques
Discussions
Open Access
EGU

[PM] evolution is given relatively, as a percentage of [PM] max, for 2 experiments with low (Figure 9b) and high (Figure 9c) initial particle surface. The first curve (Figure 9b) shows slow [PM] increase, with the

605 maximum reached after 450 min. The second curve (Figure 9c) however shows a fast evolution, with an increase occurring during 105 minutes. This fast condensation seems to be mostly determined by the high particle surface available.

Other than condensation, nucleation and coagulation are 2 processes that can have important effects on particle concentrations and distributions. Both of those processes are investigated, and results are shown in Figure 10.



610

**Figure 10: Evolution with time of the particles [PN$_i$] in certain diameter bins during 2 hours. Figures (a) and (b) show particles in the bins 18.1 nm (black) and 20.2 nm (light grey), for experiments with the vehicle D5 in MW conditions with an initial [PN] of $9.1\times10^3$ #.cm$^{-3}$ and with the vehicle D4 in UC conditions with an initial [PN] of $2.8\times10^4$ #.cm$^{-3}$, respectively. Figure (c) shows particles in the bins 18.1 nm (black), 46.1 nm (light grey) and 250.3 nm (dark grey) with**
615 **the vehicle D2 in MW conditions with an initial [PN] of $1.3\times10^5$ #.cm$^{-3}$. Figure (d) shows particles in the bins 18.1 nm (black), 113.4 nm (light grey) and 385.4 nm (dark grey) with the vehicle D1 in MW conditions with an initial [PN] of $2.5\times10^5$ #.cm$^{-3}$.**
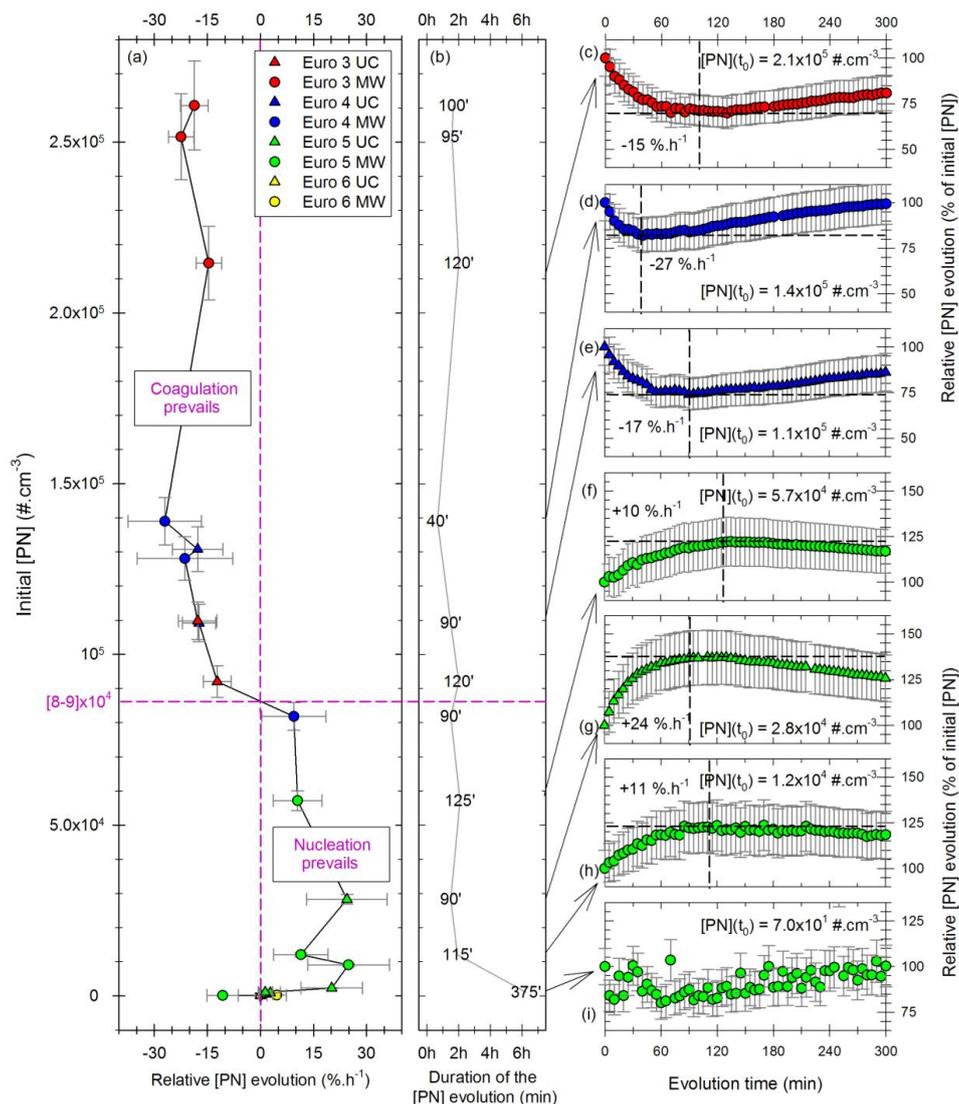
Figure 10a and Figure 10b show the evolution of small particles (in the bins centered at 18.1 and 20.2 nm), for 2 experiments with respective initial [PN] of $9.1\times10^3$ #.cm$^{-3}$ and $2.8\times10^4$ #.cm$^{-3}$. In both cases, concentrations

620 increase during the first 30 to 60 minutes of the evolution. The increase of particles with such small diameters could indicate the occurrence of nucleation or evaporation of organic compounds as particles are diluted into the chamber.

Figure 10c and Figure 10d give the evolution of the particles in 3 diameter bins, for experiments with initial [PN] of $1.3 \times 10^5$ #.cm$^{-3}$ and $2.5 \times 10^5$ #.cm$^{-3}$ respectively. In Figure 10c, the concentration of the particles in the bin

625     46.1 nm decrease rapidly during 20 to 30 minutes. Simultaneously, the concentration of larger particles (in the bin 250.3 nm) increases. This seems to indicate that particles around 46.1 nm coagulate to form larger particles. The smaller particles (around 18.1 nm) have a constant concentration. Assuming that those particles should also undergo the process of coagulation, their constant concentration could be explained by the process of nucleation. It would compensate the loss due to coagulation. It could also be compensated by evaporation of organics from

630     larger particles. This last explanation is however unlikely since total mass tends to increase and concentrations of larger particles also increase. The same trends are observed in Figure 10d, with coagulation of larger particles (around 113.4 nm) forming particles with diameters around 385.4 nm. In both cases (Figure 10c and Figure 10d), both nucleation and coagulation seem to have effects on particles.

As those 2 processes impact the total number of particles, the conditions in which they occur are investigated

635     with regards to total [PN] evolutions. For some experiments, [PN] would start by increasing, probably due to nucleation or evaporation of organic materials from ultrafine particles. [PN] can also decrease, thus showing that coagulation is the dominant process. Figure 11 shows the [PN] evolution (at the beginning of the evolution) as a function of initial [PN], and the time after which this evolution is completed. It also illustrates the different profiles that [PN] evolutions can have for several initial PN concentrations.

640

**Figure 11: Evolutions of total [PN] for the vehicles of all Euro norms (Euro 3 in red; Euro 4 in blue; Euro 5 in green; Euro 6 in yellow) and in both UC (triangles) and MW (circles) driving. Figure (a) on the y-axis the initial particle concentration, plotted versus the [PN] evolution, expressed in % of the initial concentration per hour. The horizontal pink dashed line shows the concentration for which it is estimated that the [PN] evolution trend changes between positive and negative (separated with the vertical pink dashed line). Figure (b) gives on the same vertical scale the time in minutes after which the [PN] evolution is completed. Figures (c) to (i) show examples of such [PN] evolutions with time, expressed relatively as a percentage of initial [PN], for several initial concentrations ranging between $7.0\times10^{1}$ and $2.1\times10^{5}$ #.cm$^{-3}$. The vertical dashed lines indicate the time at which the [PN] evolution stops or changes, with the percentage of initial [PN] reached at this time shown by the horizontal dashed line, and with the average hourly evolution during this period.**

645

650

Figure 11a shows that at low initial PN concentrations, [PN] evolution is not significant, and is either positive or negative, but remains low. Figure 11i shows an evolution with low initial concentration. [PN] remains quite steady during the 5 hours of evolutions. When initial [PN] increases, PN concentrations increase as well, up to

24 %.h$^{-1}$. This can occur between 1h30 and 2h. During this period of time, nucleation seems to have an important effect, increasing particle number. However, nucleation alone is not likely to occur during 2 hours. This increase can also be explained by the growth of small particles (formed at the beginning of the evolution) that became detectable in the SMPS range. Figure 11f, Figure 11g and Figure 11h show relative [PN] evolution with initial [PN] in the range [1-8]×10$^4$ #.cm$^{-3}$, and show medium to high particle increase. When initial particle concentration goes over [8-9]×10$^4$ #.cm$^{-3}$, the main evolution becomes negative. It remains negative during 40 to 120 minutes. It can reach -27 %.h$^{-1}$, clearly showing that coagulation is occurring. Figure 11c, Figure 11d and Figure 11e give examples of the [PN] decrease for those high PN initial concentration conditions.

There seems to be a breakthrough around [8-9]×10$^4$ #.cm$^{-3}$, where the evolution trend changes. The equivalent surface concentrations are [1.2-2]×10$^{-4}$ cm$^2$.cm$^{-3}$. Under this threshold, the particle number increase prevails, partially due to nucleation. This is consistent with Ning and Sioutas (2010), who show that organic vapors nucleate more easily when particle concentrations are low, and condense more easily when particle concentrations are high. This is also consistent with Figure 8, which shows that high initial [PN] leads to higher hourly [PM] increases. Above this threshold, particle number decreases over time, and coagulation becomes important, and the most significant process affecting particle number.

These results are in good agreement with tunnel measurements performed by Imhof et al. (2006). They showed that nucleation would occur more easily under low traffic density (e.g. with lower initial particle concentrations). They also showed that PN nucleation mode concentrations decrease when soot mode particle concentrations are high. Moreover, they found that nucleation mode particles increase until the surface area of soot particles reaches a threshold of 5×10$^{-5}$ cm$^2$.cm$^{-3}$. This threshold found experimentally in 2 tunnels is close (factor 2-4) to the one found in this study ([1.2-2]×10$^{-4}$ cm$^2$.cm$^{-3}$) in laboratory conditions. Finally, Imhof et al. (2006) found similar trends of traffic influence on particle evolutions as in this study. Condensation is more likely to occur in the presence of highly particle-emitting vehicles. Nucleation may be more important when traffic is composed of less polluting vehicles. Results of this study show that the processes affecting particle evolutions is greatly influenced by atmospheric concentrations, which is dependent on traffic density and fleet composition.

### 4.    Conclusion

This study presents the characterization of a new 8 m$^3$ environmental chamber with Teflon walls, meant to study the physical evolution of primary pollutants emitted by road traffic. A new size-dependent method to correct particle losses due to leakage and wall deposition was developed and applied. It accounts for experiment-to-experiment variations. It consists in 4 steps, using the [BC] decay and wall loss coefficients from the theory of Crump and Seinfeld (1981). These 2 complementary parts are in good agreement. The total loss coefficients $\alpha+\beta_{ke}{}^{mean}$ of "charged walls" experiments are in the range [4.19-11.05]×10$^{-3}$ min$^{-1}$ for diesel and [2.04-5.01]×10$^{-3}$ min$^{-1}$ for gasoline. For "neutral walls" experiments, they are in the range [1.25-4.09]×10$^{-3}$ min$^{-1}$ for diesel, [0.93-3.93]×10$^{-3}$ min$^{-1}$ for gasoline and [0.63-1.01]×10$^{-3}$ min$^{-1}$ for ammonium sulphate. The wall charges appear to be the most important factor affecting particle wall losses. Results of wall losses obtained from ammonium sulphate particle experiments show similar trends as those found in the literature for a chamber of comparable size.

EFs of PN, PM, BC and IVOCs for Euro 3 to Euro 6 diesel vehicles were studied in detail in order to understand their role on particle evolution in dark conditions. For non-DPF vehicles (D1 and D2), IVOC emissions are

dominated by n- and b- alkanes, (64 %), followed by cycloalkanes (14 %) and aromatics (16 %). For the cat DPF

vehicle (D5), alkanes represent 78 % of IVOCs, followed by cycloalkanes (19 %) and then aromatics (2 %). For

695 the vehicles with add DPFs (D3 and D6), only alkanes were identified in the IVOCs.

Moreover, this study presents results of evolution in the dark of particles emitted by diesel passenger cars. It is shown that [PM] increase can reach 17 %.h$^{-1}$, without the effects of photochemistry. [PM] increase appear to be correlated with initial [PN]. The [PM] increase of older diesel vehicles (Euro 3 and Euro 4) is enhanced in comparison to modern vehicles. This is due to their higher emissions of BC, PN and PM, compared to

700 DPF-equipped vehicles, as well as their emissions of IVOCs. Also, the condensation process is shown to be highly dependent on the available particle surface. Condensation is 4 times faster when the available surface is multiplied by 3. Finally, this study shows that the [PN] decrease (by coagulation) or [PN] increase (by nucleation or condensation on particles below 14 nm) is dependent on the particle concentration. For initial [PN] below [8-9]$\times10^4$ #.cm$^{-3}$, nucleation or condensation on particles below 14 nm are probably the main processes affecting

705 particle number. Above this threshold, coagulation prevails, due to higher probability for particles to collide. This is also explained by the fact that at high PN concentrations, gas-phase organics are more likely to condense onto preexisting particles than to nucleate.

Results found in this study under laboratory conditions are in good agreement with tunnel observations described in the literature. They can help better understand the conditions under which physical processes are more likely

710 to occur. They can be applied to several conditions in the dark, such as winter rush hours or tunnel evolutions.

*Data availability*. All data from this study are available from the authors upon request.

*Supplement*.

715

*Author contribution*. YL, BD, CF, KS, CL and BV designed the research. YL, CL and BV performed and analyzed the characterization experiments. YL and BV performed and analyzed the emission and evolution experiments. CF, LF and BV performed the ATD-GC-MS analysis. EK, BTR, BD contributed to the experimental set up and the experimental procedure. PT and PP drove the cars and helped with experimental set

720 up. BV synthesized all the data and wrote the paper with contributions from CL, VC, BD, EK, BTR, KS, CF and YL.

*Competing interests*. The authors declare that they have no conflict of interest.

725 *Acknowledgements*.

Atmospheric
Measurement
Techniques

Discussions

730    **References**

André, M., 2004. The ARTEMIS European driving cycles for measuring car pollutant emissions. Science of The Total Environment 334–335, 73–84. https://doi.org/10.1016/j.scitotenv.2004.04.070

André, M., Roche, A-L., Bourcier, L., 2014. Statistiques de parcs et trafic pour le calcul des émissions de polluants des transports routiers en France. IFSTTAR.

735    Andreae, M.O., Gelencser, A., 2006. Black carbon or brown carbon? The nature of light-absorbing carbonaceous aerosols. Atmos. Chem. Phys. 18.

Babar, Z.B., Park, J.-H., Kang, J., Lim, H.-J., 2017. Characterization of a Smog Chamber for Studying Formation and Physicochemical Properties of Secondary Organic Aerosol. Aerosol Air Qual. Res. 16, 3102–3113. https://doi.org/10.4209/aaqr.2015.10.0580

740    Barone, T.L., Lall, A.A., Storey, J.M.E., Mulholland, G.W., Prikhodko, V.Y., Frankland, J.H., Parks, J.E., Zachariah, M.R., 2011. Size-Resolved Density Measurements of Particle Emissions from an Advanced Combustion Diesel Engine: Effect of Aggregate Morphology. Energy & Fuels 25, 1978–1988. https://doi.org/10.1021/ef200084k

Charan, S.M., Kong, W., Flagan, R.C., Seinfeld, J.H., 2018. Effect of particle charge on aerosol dynamics in 745    Teflon environmental chambers. Aerosol Science and Technology 52, 854–871. https://doi.org/10.1080/02786826.2018.1474167

Chen, T., Liu, Y., Chu, B., Liu, C., Liu, J., Ge, Y., Ma, Q., Ma, J., He, H., 2019. Differences of the oxidation process and secondary organic aerosol formation at low and high precursor concentrations. Journal of Environmental Sciences 79, 256–263. https://doi.org/10.1016/j.jes.2018.11.011

750    Chu, B., Liu, Y., Ma, Q., Ma, J., He, H., Wang, G., Cheng, S., Wang, X., 2016. Distinct potential aerosol masses under different scenarios of transport at a suburban site of Beijing. Journal of Environmental Sciences 39, 52–61. https://doi.org/10.1016/j.jes.2015.11.003

Corner, J., Pendlebury, E.D., 1951. The Coagulation and Deposition of a Stirred Aerosol. Proceedings of the Physical Society. Section B 64, 645–654. https://doi.org/10.1088/0370-1301/64/8/304

755    Crump, J.G., Flagan, R.C., Seinfeld, J.H., 1982. Particle Wall Loss Rates in Vessels. Aerosol Science and Technology 2, 303–309. https://doi.org/10.1080/02786828308958636

Crump, J.G., Seinfeld, J.H., 1981. Turbulent deposition and gravitational sedimentation of an aerosol in a vessel of arbitrary shape. Journal of Aerosol Science 12, 405–415. https://doi.org/10.1016/0021-8502(81)90036-7

760    Drozd, G.T., Zhao, Y., Saliba, G., Frodin, B., Maddox, C., Oliver Chang, M.-C., Maldonado, H., Sardar, S., Weber, R.J., Robinson, A.L., Goldstein, A.H., 2019. Detailed Speciation of Intermediate Volatility and Semivolatile Organic Compound Emissions from Gasoline Vehicles: Effects of Cold-Starts and Implications for Secondary Organic Aerosol Formation. Environ. Sci. Technol. 53, 1706–1714. https://doi.org/10.1021/acs.est.8b05600

765    EEA, 2020. Average age of road vehicles per country — European Environment Agency [WWW Document]. URL https://www.eea.europa.eu/data-and-maps/daviz/average-age-of-road-vehicles-6#tab-chart_1 (accessed 11.6.20).

Giechaskiel, B., Ntziachristos, L., Samaras, Z., Scheer, V., Casati, R., Vogt, R., 2005. Formation potential of vehicle exhaust nucleation mode particles on-road and in the laboratory. Atmospheric Environment 39, 770    3191–3198. https://doi.org/10.1016/j.atmosenv.2005.02.019

Grieshop, A.P., Logue, J.M., Donahue, N.M., Robinson, A.L., 2009. Laboratory investigation of photochemical oxidation of organic aerosol from wood fires 1: measurement and simulation of organic aerosol evolution. Atmospheric Chemistry and Physics 9, 1263–1277. https://doi.org/10.5194/acp-9-1263-2009

Harrison, R.M., Rob MacKenzie, A., Xu, H., Alam, M.S., Nikolova, I., Zhong, J., Singh, A., Zeraati-Rezaei, S., 775    Stark, C., Beddows, D.C.S., Liang, Z., Xu, R., Cai, X., 2018. Diesel exhaust nanoparticles and their behaviour in the atmosphere. Proc. R. Soc. A 474, 20180492. https://doi.org/10.1098/rspa.2018.0492

Hennigan, C.J., Miracolo, M.A., Engelhart, G.J., May, A.A., Presto, A.A., Lee, T., Sullivan, A.P., McMeeking, G.R., Coe, H., Wold, C.E., Hao, W.-M., Gilman, J.B., Kuster, W.C., de Gouw, J., Schichtel, B.A., Collett, J.L., Kreidenweis, S.M., Robinson, A.L., 2011. Chemical and physical transformations of 780    organic aerosol from the photo-oxidation of open biomass burning emissions in an environmental chamber. Atmos. Chem. Phys. 11, 7669–7686. https://doi.org/10.5194/acp-11-7669-2011

Huang, R.-J., Zhang, Y., Bozzetti, C., Ho, K.-F., Cao, J.-J., Han, Y., Daellenbach, K.R., Slowik, J.G., Platt, S.M., Canonaco, F., Zotter, P., Wolf, R., Pieber, S.M., Bruns, E.A., Crippa, M., Ciarelli, G., Piazzalunga, A., Schwikowski, M., Abbaszade, G., Schnelle-Kreis, J., Zimmermann, R., An, Z., Szidat, 785    S., Baltensperger, U., Haddad, I.E., Prévôt, A.S.H., 2014. High secondary aerosol contribution to particulate pollution during haze events in China. Nature 514, 218–222. https://doi.org/10.1038/nature13774

IARC, 2016. Outdoor aur pollution (No. 109). IARC.

790     Imhof, D., Weingartner, E., Prévôt, A., Ordóñez, C., Kurtenbach, R., Wiesen, P., Rodler, J., Sturm, P., Mccrae,
            I., Ekström, M., Baltensperger, U., 2006. Aerosol and NOx emission factors and submicron particle
            number size distributions in two road tunnels with different traffic regimes. Atmos. Chem. Phys. 17.
        Jeong, C.-H., Evans, G.J., Healy, R.M., Jadidian, P., Wentzell, J., Liggio, J., Brook, J.R., 2015. Rapid physical
            and chemical transformation of traffic-related atmospheric particles near a highway. Atmospheric
            Pollution Research 6, 662–672. https://doi.org/10.5094/APR.2015.075
795     Kozawa, K.H., Winer, A.M., Fruin, S.A., 2012. Ultrafine particle size distributions near freeways: Effects of
            differing     wind     directions     on     exposure.     Atmospheric     Environment     63,     250–260.
            https://doi.org/10.1016/j.atmosenv.2012.09.045
        La, Y.S., Camredon, M., Ziemann, P.J., Valorso, R., Matsunaga, A., Lannuque, V., Lee-Taylor, J., Hodzic, A.,
            Madronich, S., Aumont, B., 2016. Impact of chamber wall loss of gaseous organic compounds on
800         secondary organic aerosol formation: explicit modeling of SOA formation from alkane and alkene
            oxidation. Atmos. Chem. Phys. 16, 1417–1431. https://doi.org/10.5194/acp-16-1417-2016
        Lambe, A.T., Onasch, T.B., Massoli, P., Croasdale, D.R., Wright, J.P., Ahern, A.T., Williams, L.R., Worsnop,
            D.R., Brune, W.H., Davidovits, P., 2011. Laboratory studies of the chemical composition and cloud
            condensation nuclei (CCN) activity of secondary organic aerosol (SOA) and oxidized primary organic
805         aerosol (OPOA). Atmos. Chem. Phys. 16.
        Leskinen, A., Yli-Pirilä, P., Kuuspalo, K., Sippula, O., Jalava, P., Hirvonen, M.-R., Jokiniemi, J., Virtanen, A.,
            Komppula, M., Lehtinen, K.E.J., 2015. Characterization and testing of a new environmental chamber.
            Atmospheric Measurement Techniques 8, 2267–2278. https://doi.org/10.5194/amt-8-2267-2015
        Louis, C., Liu, Y., Martinet, S., D'Anna, B., Valiente, A.M., Boreave, A., R'Mili, B., Tassel, P., Perret, P.,
810         André, M., 2017. Dilution effects on ultrafine particle emissions from Euro 5 and Euro 6 diesel and
            gasoline     vehicles.     Atmospheric     Environment     169,     80–88.
            https://doi.org/10.1016/j.atmosenv.2017.09.007
        Lu, J., Ge, X., Liu, Y., Chen, Y., Xie, X., Ou, Y., Ye, Z., Chen, M., 2019. Significant secondary organic aerosol
            production from aqueous-phase processing of two intermediate volatility organic compounds.
815         Atmospheric Environment 211, 63–68. https://doi.org/10.1016/j.atmosenv.2019.05.014
        Lu, Q., Zhao, Y., Robinson, A.L., 2018. Comprehensive organic emission profiles for gasoline, diesel, and gas-
            turbine engines including intermediate and semi-volatile organic compound emissions. Atmos. Chem.
            Phys. 18, 17637–17654. https://doi.org/10.5194/acp-18-17637-2018
        Morawska, L., Ristovski, Z., Jayaratne, E.R., Keogh, D.U., Ling, X., 2008. Ambient nano and ultrafine particles
820         from motor vehicle emissions: Characteristics, ambient processing and implications on human
            exposure. Atmospheric Environment 42, 8113–8138. https://doi.org/10.1016/j.atmosenv.2008.07.050
        Nah, T., McVay, R.C., Pierce, J.R., Seinfeld, J.H., Ng, N.L., 2017. Constraining uncertainties in particle-wall
            deposition correction during SOA formation in chamber experiments. Atmospheric Chemistry and
            Physics 17, 2297–2310. https://doi.org/10.5194/acp-17-2297-2017
825     Ning, Z., Sioutas, C., 2010. Atmospheric Processes Influencing Aerosols Generated by Combustion and the
            Inference of Their Impact on Public Exposure: A Review. Aerosol Air Qual. Res. 10, 43–58.
            https://doi.org/10.4209/aaqr.2009.05.0036
        Nomura, Y., Hopke, P.K., Fitzgerald, B., Mesbah, B., 1997. Deposition of Particles in a Chamber as a Function
            of     Ventilation     Rate.     Aerosol     Science     and     Technology     27,     62–72.
830         https://doi.org/10.1080/02786829708965458
        Okuyama, K., Kousaka, Y., Yamamoto, S., Hosokawa, T., 1986. Particle loss of aerosols with particle diameters
            between 6 and 2000 nm in stirred tank. Journal of Colloid and Interface Science 110, 214–223.
            https://doi.org/10.1016/0021-9797(86)90370-X
        Papapostolou, V., Lawrence, J.E., Diaz, E.A., Wolfson, J.M., Ferguson, S.T., Long, M.S., Godleski, J.J.,
835         Koutrakis, P., 2011. Laboratory evaluation of a prototype photochemical chamber designed to
            investigate the health effects of fresh and aged vehicular exhaust emissions. Inhalation Toxicology 23,
            495–505. https://doi.org/10.3109/08958378.2011.587034
        Pathak, R.K., Stanier, C.O., Donahue, N.M., Pandis, S.N., 2007. Ozonolysis of α-pinene at atmospherically
            relevant concentrations: Temperature dependence of aerosol mass fractions (yields). Journal of
840         Geophysical Research: Atmospheres 112. https://doi.org/10.1029/2006JD007436
        Pierce, J.R., Engelhart, G.J., Hildebrandt, L., Weitkamp, E.A., Pathak, R.K., Donahue, N.M., Robinson, A.L.,
            Adams, P.J., Pandis, S.N., 2008. Constraining Particle Evolution from Wall Losses, Coagulation, and
            Condensation-Evaporation in Smog-Chamber Experiments: Optimal Estimation Based on Size
            Distribution     Measurements.     Aerosol     Science     and     Technology     42,     1001–1015.
845         https://doi.org/10.1080/02786820802389251
        Platt, S.M., El Haddad, I., Zardini, A.A., Clairotte, M., Astorga, C., Wolf, R., Slowik, J.G., Temime-Roussel, B.,
            Marchand, N., Ježek, I., Drinovec, L., Močnik, G., Möhler, O., Richter, R., Barmet, P., Bianchi, F.,
            Baltensperger, U., Prévôt, A.S.H., 2013. Secondary organic aerosol formation from gasoline vehicle

Atmospheric
Measurement
Techniques
Discussions

emissions in a new mobile environmental reaction chamber. Atmospheric Chemistry and Physics 13, 9141–9158. https://doi.org/10.5194/acp-13-9141-2013

Rivas, I., Beddows, D.C.S., Amato, F., Green, D.C., Järvi, L., Hueglin, C., Reche, C., Timonen, H., Fuller, G.W., Niemi, J.V., Pérez, N., Aurela, M., Hopke, P.K., Alastuey, A., Kulmala, M., Harrison, R.M., Querol, X., Kelly, F.J., 2020. Source apportionment of particle number size distribution in urban background and traffic stations in four European cities. Environment International 135, 105345. https://doi.org/10.1016/j.envint.2019.105345

Sartelet, K., Zhu, S., Moukhtar, S., André, M., André, J.M., Gros, V., Favez, O., Brasseur, A., Redaelli, M., 2018. Emission of intermediate, semi and low volatile organic compounds from traffic and their impact on secondary organic aerosol concentrations over Greater Paris. Atmospheric Environment 180, 126–137. https://doi.org/10.1016/j.atmosenv.2018.02.031

Sbai, S.E., Li, C., Boreave, A., Charbonnel, N., Perrier, S., Vernoux, P., Bentayeb, F., George, C., Gil, S., 2020. Atmospheric photochemistry and secondary aerosol formation of urban air in Lyon, France. Journal of Environmental Sciences 99, 311–323. https://doi.org/10.1016/j.jes.2020.06.037

Schnell, M., Cheung, C.S., Leung, C.W., 2006. Investigation on the coagulation and deposition of combustion particles in an enclosed chamber with and without stirring. Journal of Aerosol Science 37, 1581–1595. https://doi.org/10.1016/j.jaerosci.2006.06.001

Seinfeld, J.H., Pandis, S.N., 2016. Atmospheric chemistry and physics: from air pollution to climate change.

Totton, T.S., Chakrabarti, D., Misquitta, A.J., Sander, M., Wales, D.J., Kraft, M., 2010. Modelling the internal structure of nascent soot particles. Combustion and Flame 157, 909–914. https://doi.org/10.1016/j.combustflame.2009.11.013

TSI, 2010. Aerosol Instrument Manager Software for Scanning Mobility Particle Sizer (SMPS) Spectrometer User's Manual.

Verheggen, B., Mozurkewich, M., 2006. An inverse modeling procedure to determine particle growth and nucleation rates from measured aerosol size distributions. Atmos. Chem. Phys. 16.

Wang, N., Jorga, S., Pierce, J., Donahue, N., Pandis, S., 2018a. Particle Wall-loss Correction Methods in Smog Chamber Experiments. Atmospheric Measurement Techniques Discussions 1–29. https://doi.org/10.5194/amt-2018-175

Wang, N., Kostenidou, E., Donahue, N.M., Pandis, S.N., 2018b. Multi-generation chemical aging of &lt;i&gt;α&lt;/i&gt;-pinene ozonolysis products by reactions with OH. Atmos. Chem. Phys. 18, 3589–3601. https://doi.org/10.5194/acp-18-3589-2018

Wang, X., Liu, T., Bernard, F., Ding, X., Wen, S., Zhang, Y., Zhang, Z., He, Q., Lü, S., Chen, J., Saunders, S., Yu, J., 2014. Design and characterization of a smog chamber for studying gas-phase chemical mechanisms and aerosol formation. Atmospheric Measurement Techniques 7, 301–313. https://doi.org/10.5194/amt-7-301-2014

Weitkamp, E.A., Sage, A.M., Pierce, J.R., Donahue, N.M., Robinson, A.L., 2007. Organic Aerosol Formation from Photochemical Oxidation of Diesel Exhaust in a Smog Chamber. Environmental Science & Technology 41, 6969–6975. https://doi.org/10.1021/es070193r

Xu, R., Alam, M.S., Stark, C., Harrison, R.M., 2020. Behaviour of traffic emitted semi-volatile and intermediate volatility organic compounds within the urban atmosphere. Science of The Total Environment 720, 137470. https://doi.org/10.1016/j.scitotenv.2020.137470

Zhang, K.M., Wexler, A.S., 2004. Evolution of particle number distribution near roadways—Part I: analysis of aerosol dynamics and its implications for engine emission measurement. Atmospheric Environment 38, 6643–6653. https://doi.org/10.1016/j.atmosenv.2004.06.043

Zhang, K.M., Wexler, A.S., Zhu, Y.F., Hinds, W.C., Sioutas, C., 2004. Evolution of particle number distribution near roadways. Part II: the 'Road-to-Ambient' process. Atmospheric Environment 38, 6655–6665. https://doi.org/10.1016/j.atmosenv.2004.06.044

Zhao, Y., Lambe, A.T., Saleh, R., Saliba, G., Robinson, A.L., 2018. Secondary Organic Aerosol Production from Gasoline Vehicle Exhaust: Effects of Engine Technology, Cold Start, and Emission Certification Standard. Environ. Sci. Technol. 52, 1253–1261. https://doi.org/10.1021/acs.est.7b05045

Zhao, Y., Nguyen, N.T., Presto, A.A., Hennigan, C.J., May, A.A., Robinson, A.L., 2016. Intermediate Volatility Organic Compound Emissions from On-Road Gasoline Vehicles and Small Off-Road Gasoline Engines. Environmental Science & Technology 50, 4554–4563. https://doi.org/10.1021/acs.est.5b06247

Zhao, Y., Nguyen, N.T., Presto, A.A., Hennigan, C.J., May, A.A., Robinson, A.L., 2015. Intermediate Volatility Organic Compound Emissions from On-Road Diesel Vehicles: Chemical Composition, Emission Factors, and Estimated Secondary Organic Aerosol Production. Environ. Sci. Technol. 49, 11516–11526. https://doi.org/10.1021/acs.est.5b02841

Zhu, J., Penner, J.E., Lin, G., Zhou, C., Xu, L., Zhuang, B., 2017. Mechanism of SOA formation determines magnitude of radiative effects. Proc Natl Acad Sci USA 114, 12685–12690. https://doi.org/10.1073/pnas.1712273114

910 **Appendix A**

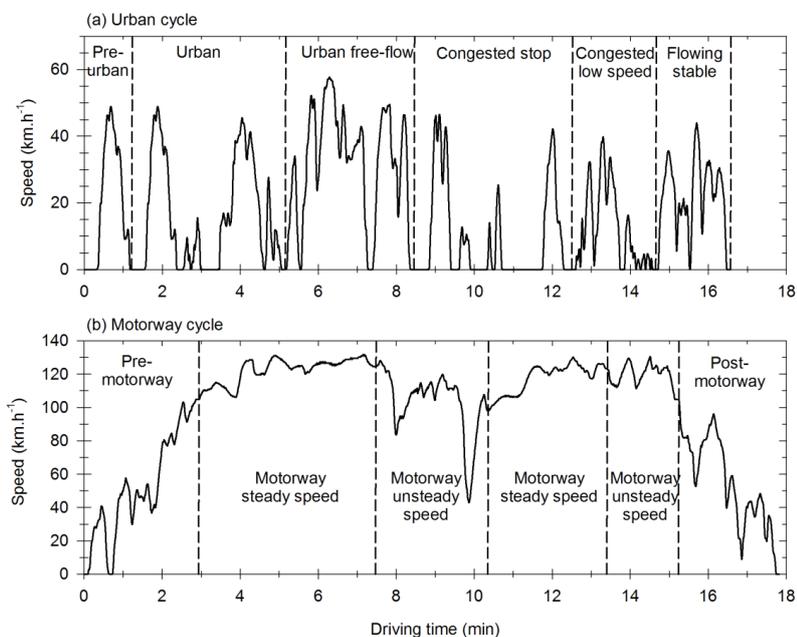Below are shown the speed profiles of the Artemis Urban and Artemis Motorway cycles.



**Figure A1: Speed in km.h$^{-1}$ during the Artemis Urban cycle (a) and the Artemis Motorway cycle (b), with the different types of driving found in those conditions.**

915 **Appendix B**

Below are listed the constants taken for the calculation of $\beta(D_p)$:

- $k_B = 1.381 \times 10^{-23}$ J.K$^{-1}$ the Boltzmann constant
- $T$ (K) the temperature in the chamber for each experiment
- $\mu = 1.8 \times 10^{-5}$ kg.m$^{-1}$.s$^{-1}$ the viscosity of air
920 - $\rho_p = 1.2$ g.cm$^{-3}$ the particle density
- $g = 9.81$ m.s$^{-2}$ the g-force
- $\lambda = 6.51$ nm the mean-free path of air

Atmospheric
Measurement
Techniques

Open Access

Discussions

EGU

**Appendix C**

925 **Table C1: Emission factors in mg.km⁻¹ of: linear (n-) and branched (b-) alkanes with carbon number below between 12 and 22 (C12-C22), of naphthalene, cycloalkanes and aromatics measured with the ATD-GC-MS method. The sum of those EFs gives the IVOC EFs. Emission factors of n- and b- alkanes with carbon number above 22. Emission factors of NMHCs measured by flame ionization detection. Emissions below quantification limit are indicated as "< QL". Ratio of IVOC/NMHC expressed as % of NMHCs. Results are shown for vehicles D1 (Euro 3), D2 (Euro 4), D3 (Euro 5 add DPF), D5 (Euro 5 cat DPF) and D6 (Euro 6 add DPF and SCR), in both UC and MW conditions.**

| Vehicle | D1 | | D2 | | D3 (add DPF) | | D5 (cat DPF) | | D6 (add DPF and SCR) | |
|---|---|---|---|---|---|---|---|---|---|---|
| Cycle | UC | MW | UC | MW | UC | MW | UC | MW | UC | MW |
| n-/b- alkanes C12-C22 (mg.km⁻¹) | 1.05 ± 0.31 | 1.25 ± 0.08 | 0.19 ± 0.03 | 0.55 ± 0.48 | 0.12 ± 0.02 | 0.02 ± 0.01 | 0.72 ± 0.10 | 0.65 ± 0.68 | 0.04 ± 0.04 | 0.02 ± 0.02 |
| Naphthalene (mg.km⁻¹) | 0.03 ± 0.03 | 0.06 ± 0.02 | 0.04 ± 0.01 | 0.09 ± 0.05 | <QL | <QL | 0.01 ± 0.01 | <QL | <QL | <QL |
| Cycloalkanes (mg.km⁻¹) | 0.2 ± 0.10 | 0.22 ± 0.01 | 0.05 ± 0.04 | 0.16 ± 0.16 | <QL | <QL | 0.29 ± 0.06 | 0.08 ± 0.12 | <QL | <QL |
| Aromatics (mg.km⁻¹) | 0.04 ± 0.49 | 0.05 ± 0.13 | 0.23 ± 0.40 | 0.12 ± 0.74 | <QL | <QL | 0.04 ± 0.17 | 0.01 ± 0.82 | <QL | <QL |
| IVOCs (mg.km⁻¹) | 1.32 ± 0.93 | 1.58 ± 0.24 | 0.5 ± 0.48 | 0.92 ± 1.42 | 0.12 ± 0.04 | 0.02 ± 0.01 | 1.06 ± 0.34 | 0.74 ± 1.62 | 0.04 ± 0.08 | 0.02 ± 0.04 |
| n-/b- alkanes C>22 (mg.km⁻¹) | 1.56 ± 1.26 | 1.27 ± 1.35 | 0.26 ± 0.30 | 0.66 ± 0.01 | 0.35 ± 0.06 | 0.29 ± 0.43 | 1.46 ± 1.47 | 2.63 ± 3.17 | 0.17 ± 0.12 | 0.2 ± 0.24 |
| NMHCs (mg.km⁻¹) | 102.93 ± 39.43 | 22.82 ± 2.79 | 52.31 ± 27.29 | 18.38 ± 2.29 | 22.68 ± 0.89 | 2.25 ± 0.53 | 113.37 ± 2.00 | 3.01 ± 4.14 | 5.18 ± 0.96 | No data |
| IVOC/NMHC (%) | 1.28 ± 0.48 | 6.91 ± 0.59 | 0.96 ± 0.77 | 5.00 ± 4.02 | 0.54 ± 0.09 | 0.88 ± 0.21 | 0.93 ± 0.15 | 24.73 ± 27.10 | 0.79 ± 0.78 | No data |

\* QL = Quantification Limit